New Synthetic Mimics for Heteroatom

Polycyclic Aromatic Hydrocarbon-based Cosmic Dust

Derek H. H. Chan [a], Emma E. Brotherton [a], Steven P. Armes [a,*]

Jessica L. Wills [c], Jon D. Tandy [b], Mark J. Burchell [c], Penelope J. Wozniakiewicz [c] and Luke S. Alesbrook[c]

a. Dainton Building, Department of Chemistry, University of Sheffield, Brook Hill, Sheffield, South Yorkshire, S3 7HF, UK.

b. School of Natural Sciences, University of Kent, Canterbury CT2 7NZ, UK.

c. School of Engineering, Mathematics and Physics, University of Kent, Canterbury, Kent CT2 7NH, UK.

Abstract. Herein we report the preparation of new synthetic mimics for nitrogen-based polycyclic aromatic hydrocarbon (PANH) cosmic dust particles. From a small library of candidate molecules, we chose to study benzo[*h*]quinoline (m.p. = 51°C). This simple PANH was processed by hot emulsification in the presence of a suitable water-soluble polymeric emulsifier: high shear homogenization at 55°C converted the initial millimeter-sized drops into much finer molten oil droplets. The mean droplet diameter was readily controlled from 12 to 273 µm by adjusting the shear rate. Subsequent cooling to 20°C led to crystallization and the formation of polydisperse benzo[*h*]quinoline microparticles. Interestingly, the nature of the polymeric emulsifier has a significant influence on the final microparticle morphology. Distinctly anisotropic microparticles were obtained using poly(vinyl alcohol), whereas the desired spherical morphology was produced when using Morwet D-425. Next, a melting point diagram constructed for a series of binary mixtures of benzo[*h*]quinoline and phenanthrene indicated a eutectic composition of 65 mol% benzo[*h*]quinoline, with a corresponding melting point of just 37°C. Accordingly, hot emulsification processing was again employed to produce a series of 65:35 benzo[*h*]quinoline/phenanthrene hybrid microparticles of 19 to 438 µm diameter. In this case, only the PVA emulsifier produced the desired spherical morphology. These hybrid microparticles were characterized by optical/fluorescence microscopy, laser diffraction, scanning electron microscopy, ^{1}H NMR spectroscopy, and Raman microscopy. Both types of microparticles were fired in turn at aluminum foil or aerogel targets at 0.9 – 1.0 km s^{-1} using a light gas gun. Under such conditions, the microparticles simply rebounded from aluminum foil, with no signs of fragmentation or melting. In contrast, the 65:35 benzo[*h*]quinoline/phenanthrene microparticles underwent complete ablation during their aerogel capture. These new PANH synthetic mimics combined with such high-energy impact data will inform the design and calibration of cosmic dust detectors for the next generation of interplanetary unmanned spacecraft.

* Author to whom correspondence should be addressed (s.p.armes@shef.ac.uk)

Introduction

Polycyclic aromatic hydrocarbons (PAHs) are abundant throughout the known Universe. They are believed to influence the evolution of galaxies and the formation of planets and stars[1–5] and are also considered to be an important source of carbon,[4,6] which has implications for the origin of life.[7] In this context, PAH molecules have been detected in meteorites,[8] comets,[9–11] on Titan,[12] and within interplanetary cosmic dust grains.[13]

Typically, cosmic dust travels at hypervelocities (> 1 km s^{-1}). If such fast-moving dust particles impinge on a suitable metal target, their kinetic energy is often sufficient to cause molecular fragmentation and ionization, which generates a characteristic ionic plasma. This allows the chemical composition of the original dust particles to be determined by impact ionization mass spectrometry.[14–18] This principle has underpinned the design of several generations of cosmic dust detectors for a series of space missions.[19–22] For example, a detector using this method has reported the presence of salts[16] and macromolecules[17] in the icy plumes emanating from the sub-surface ocean of Enceladus, one of the moons of Saturn. Such detectors are well-suited for studies of submicron-sized cosmic dust. In principle, larger cosmic dust grains can be captured within thin foils[23,24] or ultralow-density aerogels.[23,25–27] There is considerable interest in designing next-generation synthetic mimics for cosmic dust to evaluate both their capture and *in situ* analysis in future space missions to explore the icy ocean world satellites of Jupiter and Saturn. Depending on the type of mission, dust aerogel capture experiments are likely to be performed at speeds of 0.25 to 2 km s^{-1}, while for dust detection via impact ionization the corresponding fly-by velocities are estimated to range from 5 to 17 km s^{-1}.[21,28–32]

In 2021 we demonstrated that wet ball-milling of coarse anthracene crystals enabled preparation of the first synthetic mimic for PAH-based cosmic dust.[33] Anthracene microparticles with a relatively ill-defined, non-spherical morphology were obtained and subsequently fired at an aluminum foil target at 1.87 km s^{-1} using a two-stage light gas gun.[34] Such microparticles can be coated with an ultrathin overlayer of an electrically conductive polymer (polypyrrole), which enables significantly higher hypervelocities (10-20 km s^{-1}) to be achieved using a high-voltage van der Graaff accelerator.[35] Recently, we reported the synthesis of well-defined spherical phenanthrene microparticles using a new hot emulsification route that takes advantage of the relatively low melting point of 101 °C observed for this simple PAH. More specifically, millimeter-sized molten phenanthrene droplets were initially formed within a 3:1 water/ethylene glycol mixture at 106°C. Subsequently, high-shear homogenization in the presence of a suitable water-soluble polymeric emulsifier generated a relatively fine oil-in-water emulsion. On cooling to 20°C, the emulsion droplets crystallized to form an aqueous suspension of polydisperse phenanthrene spheres, whose mean diameter could be tuned from around 25 µm to more than 250 µm simply by varying the shear rate.[36] Such microparticles were fired at an aluminum foil target using a two-stage light gas gun.[36] Moreover, the intrinsic autofluorescence exhibited by phenanthrene was used to identify its presence within the resulting impact craters using fluorescence microscopy.[36]

PAHs were first identified within the interstellar medium by Tielens *et al*., who observed a strong infrared emission band at 6.2 µm.[1] Subsequently, it has been suggested that this distinctive spectral feature is best explained in terms of nitrogen-containing PAH (or PANH) molecules.[37,38] More recently, a plausible progenitor for PAH molecules (benzonitrile) has also been detected within the interstellar medium.[39] In view of these fascinating studies, we decided to design new synthetic mimics for cosmic dust comprising *heteroatom* PAHs to supplement the purely carbon-based PAH-based mimics

described above. After due consideration of toxicity, cost and appropriate physical properties (i.e., relatively low melting point and minimal aqueous solubility) of a library of putative molecules, we decided to study benzo[*h*]quinoline (see **Scheme 1**). Importantly, this simple PANH molecule has a remarkably low melting point of 51°C. Herein we report the formation of a series of spherical benzo[*h*]quinoline microparticles via the hot emulsification processing route recently used for phenanthrene.[36] The effect of varying the stirring rate and the type of polymeric emulsifier (see **Scheme S1** for their chemical structures) on the final particle size distribution was studied using optical microscopy, laser diffraction and scanning electron microscopy. These PANH microparticles were also examined using fluorescence microscopy and a series of hybrid benzo[*h*]quinoline/phenanthrene microparticles were also prepared. Finally, selected microparticles were evaluated in preliminary hypervelocity experiments using a light gas gun.

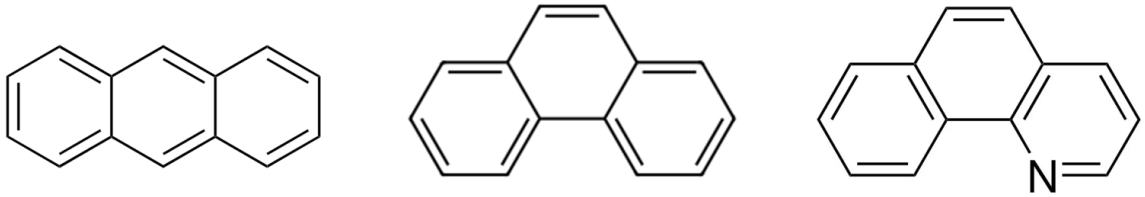

Anthracene (m.p. = 215 °C) **Phenanthrene (m.p. = 101 °C)** **Benzo[*h*]quinoline (m.p. = 51 °C)**

Scheme 1. Chemical structures and melting points of anthracene, phenanthrene and benzo[*h*]quinoline. The latter nitrogen-based PAH (or PANH) is the focus of the present study.

Experimental

Materials. Benzo[*h*]quinoline (99% purity) was purchased from TCI Chemicals (UK). Phenanthrene (98% purity) was purchased from Thermo Scientific (UK). Poly(*N*-vinyl pyrrolidone) (PNVP; nominal molecular weight = 350,000 g mol^{-1}), poly(vinyl alcohol) (PVA; nominal molecular weight = 31,000–50,000 g mol^{-1}; residual vinyl acetate content = 12 mol%) were purchased from Sigma-Aldrich (UK). Morwet D-425 was kindly provided by Syngenta (Jealotts Hill R & D site, UK). Deionized water obtained from a Elga Medica DV25 unit was used for all experiments.

Synthesis

Preparation of Spherical Benzo[h]quinoline Microparticles

A representative synthesis protocol for benzo[*h*]quinoline microparticles is as follows. Benzo[*h*]quinoline (1.0 g, 5.0% w/w), Morwet-D425 (0.20 g, 1.0% w/w) and deionized water (18.8 g) were added to a 50 mL round-bottomed flask. The flask was immersed in an oil bath set at 55 °C with an initial stirring rate of 100 rpm using an IKA Ultra-Turrax T-18 homogenizer equipped with a 10 mm dispersing tool. The benzo[*h*]quinoline crystals subsequently melted, leading to the initial formation of millimeter-sized oil drops. Magnetic stirring at either 500 or 750 rpm afforded relatively large molten droplets. High-shear homogenization of this benzo[*h*]quinoline/water mixture at 55 °C was

conducted by adjusting the stirring rate from 3,000 from 18,000 rpm for 30 seconds. The resulting hot milky-white emulsion/dispersion was vacuum-filtered using a Buchner funnel and the moist white solid was quickly redispersed in deionized water (25 mL). The final milky-white dispersion was freeze-dried to produce a fine white powder. A similar protocol was employed for the synthesis of benzo[*h*]quinoline microparticles using either PVA (0.20 g) or PNVP (0.20 g) as the emulsifier. A fixed stirring rate of 6,000 rpm was used for these latter syntheses.

Preparation of Spherical 65:35 Benzo[h]quinoline/Phenanthrene Microparticles

To prepare 20-200 μm diameter microparticles, the following protocol was used. Benzo[*h*]quinoline (0.149 g, 3.25% w/w) and phenanthrene (0.080 g, 1.75% w/w; corresponding to a composition of 65:35 benzo[*h*]quinoline/phenanthrene) were weighed into a 10 mL round-bottomed flask. PVA emulsifier (0.046 g, 1.0% w/w) and deionized water (4.313 g, 94% w/w) were added to a separate 10 mL flask and stirred overnight until the PVA was completely dissolved (if required, such solutions were heated to 40 °C to aid molecular dissolution). The flask containing the benzo[*h*]quinoline/phenanthrene mixture was immersed in an oil bath set at 55 °C until the crystals melted to form molten mm-sized oil drops. At this point, the oil bath temperature was lowered to 40 °C. The separate aqueous emulsifier solution (preheated to 40 °C) was then poured into the flask containing the molten benzo[*h*]quinoline/phenanthrene biphasic mixture. An IKA Ultra-Turrax T-18 homogenizer equipped with a 10 mm dispersing tool was lowered into the flask until the dispersing tool head was completely covered. High-shear homogenization of the benzo[*h*]quinoline/phenanthrene/water mixture was conducted for 30 seconds at a stirring rate ranging between 3,000 and 21,000 rpm. The flask containing the hot milky-white emulsion was submerged in liquid nitrogen until the sample was completely frozen. The flask was then warmed gently, and the resulting dispersion was vacuum-filtered using a Buchner funnel. The moist white solid was then freeze-dried overnight to afford a white free-flowing powder. To prepare larger (*ca*. 400 μm) 65:35 benzo[*h*]quinoline/phenanthrene microparticles, the above protocol was used but the homogenization step was conducted at a stirring rate of 500 rpm for 1 min using a magnetic stirrer. A mean particle diameter of 438 ± 120 μm was estimated by optical microscopy (50 particles were analyzed using *ImageJ* software).

Characterization Methods

Laser Diffraction Particle Size Analysis

Microparticles were analyzed using a Malvern Mastersizer 3000 laser diffraction instrument equipped with a Hydro EV wet dispersion unit, a red He-Ne laser (λ = 633 nm) and a blue LED light source (λ = 470 nm). The stirring rate was set at 1,500 rpm and the volume-average particle diameter, D (50) was calculated from the average of three measurements.

Optical Microscopy

Representative images of the microparticles were recorded using a Cole-Palmer optical microscope fitted with a Moticam camera linked to a PC with Motic Images Plus 3.0 software. [N.B. In some cases, images were recorded for molten droplets, which are significantly more transparent than the

corresponding microparticles obtained after cooling to 20 °C]. Following light gas gun experiments, the silica aerogel targets were studied by optical microscopy using a Leica M205 C microscope equipped with a Leica DMC 4500 camera.

Fluorescence microscopy

Representative images for the microparticles were recorded using a Zeiss Axio Scope A1 microscope equipped with a Zeiss Axio Cm1 camera. Fluorescence microscopy images were obtained using a LED radiation source combined with either filter set 02 (excitation λ = 365 nm, emission λ > 420 nm) or filter set 38 (excitation λ = 470 nm, emission λ = 525 nm). Additional fluorescence images were recorded of the aluminum and aerogel targets after performing the light gas gun experiments, using the fluorescence optics mode of a Leica M205 C microscope and employing a Fisher Scientific UVP Blak-Ray B-100AP/R high-intensity UV lamp (λ = 365 nm) for sample illumination.

Melting point measurements

A series of benzo[*h*]quinoline/phenanthrene binary mixtures of varying composition were weighed into 14 mL glass vials and sealed with a rubber septum. Each vial was heated using a heat gun under a constant flow of N_2 gas until the crystals completely melted. Each sample recrystallized on cooling to 20 °C. Melting points (± 0.1 °C) for the resulting series of benzo[*h*]quinoline/phenanthrene binary mixtures (*ca*. 1-2 mg) were determined using a Stuart SMP50 automatic melting point instrument at a heating rate of 2 °C min^{-1}.

Hot-stage optical microscopy

Spherical microparticles were imaged using a Zeiss Axio Scope A1 Microscope equipped with a Zeiss Axio Cm1 camera. A Linkam THMS600 heating stage (Linkam Scientific Instruments, Tadworth, UK) was mounted onto the microscope stage and attached to a T95 system controller (see **Figure S1**). The uncertainty in the measured temperature is estimated to be ± 1.0 °C. A thin copper sheet (0.15 mm thickness) was placed on the heating stage and the microparticles were carefully arranged using a microspatula. The stage was covered with three glass slides and illuminated using two LED bedside lamps (Navlinge, IKEA, UK) at an angle of approximately 45°. A heating rate of 0.5 °C min^{-1} was selected and images were recorded at 2.5x magnification at regular temperature intervals. Experiments were performed using 65:35 benzo[*h*]quinoline/phenanthrene hybrid microparticles of approximately 438 ± 120 μm diameter.

^{1}H NMR spectroscopy

^{1}H NMR spectra were recorded using a 400 MHz Bruker Avance-400 spectrometer at 298 K with 16 scans being averaged per spectrum. Spectra were recorded in d_6-acetone for the 438 ± 120 μm diameter 65:35 benzo[*h*]quinoline/phenanthrene microparticles, pure benzo[*h*]quinoline and pure phenanthrene. The integrated proton signal at 8.84 ppm assigned to the two 'bay' protons for phenanthrene was compared to the integrated proton signal at 9.02 ppm corresponding to the single C-H proton adjacent to the nitrogen atom for benzo[*h*]quinoline. An average chemical composition was determined from ten ^{1}H NMR spectra, each recorded for a *single* benzo[*h*]quinoline/phenanthrene microparticle (see **Figure S2**).

Raman microscopy

Raman spectra were acquired for *individual* microparticles using a LabRam HR Raman microscope fitted with a 600 lines/mm grating and a Peltier-cooled CCD array detector (1024 x 256 pixels). The laser excitation wavelength was 633 nm and a 25% neutral-density filter was utilized. A x10 objective was employed and the corresponding spot size was typically 4 μm, which is much smaller than the mean diameter of the microparticles. The Raman instrument was calibrated using the characteristic 519 cm^{-1} band observed for silicon wafer prior to all measurements. This protocol ensures a spectral resolution of 1-2 cm^{-1}. The spectral accumulation time varied from 2 to 5 seconds, with 20 accumulations per spectrum. Background fluorescence spectra were subtracted with the aid of Python code.

Scanning electron microscopy (SEM)

Post-shot SEM studies of aluminum foil targets were conducted using a Hitachi S3400 scanning electron microscope. An accelerating voltage of 15 kV was employed and the beam current was varied between 65 and 91 μA. An Oxford Instruments X-Max 80 mm^2 energy-dispersive X-Ray spectroscopy detector was used to map elemental compositions across individual impact craters observed at the surface of the aluminum foil targets [N.B. The aluminum foil targets were not gold-coated for such studies].

Light Gas Gun experiments

Hypervelocity impact experiments were performed using a two-stage Light Gas Gun facility at the University of Kent.[34,40] This gun fires a sabot that is loaded with milligram quantities of the microparticles and this sabot is discarded in flight. The impact speed (which is accurate to ± 4%) was determined by the difference between timing signals for the passage of the sabot through a laser light at the exit of the gun barrel and the impact of the discarded sabot on a stop plate in front of the target, which is mounted in a chamber at a pressure of 0.5 mbar. Two types of targets were used: (i) aluminum foil (type Al-1080; 99.8% purity; 100 μm thickness with a surface area of 40 mm x 40 mm and density 2712 kg m^{-3}) and (ii) an ultralow-density silica aerogel (ρ = 89 ± 1 kg m^{-3}). Such targets have been used in our prior impact experiments with PAH-based microparticles,[33,36,41] as well as for the *in situ* capture of dust particles emanating from the comet P/Wild-2 by NASA's *Stardust* mission.[23,26,27]

Results and Discussion

Synthesis and characterization of benzo[*h*]quinoline microparticles

In preliminary experiments, we took advantage of the relatively low melting point of benzo[*h*]quinoline (51°C) to convert its initial coarse crystals into first millimeter-sized drops and then much finer droplets of 12 to 273 μm diameter via hot emulsification under high shear at 55°C, see **Scheme 2**. On cooling to 20°C, such droplets recrystallize to form the desired microparticles. Unlike our recently reported preparation of phenanthrene microparticles,[36] this formulation does not require the use of ethylene glycol as a co-solvent.

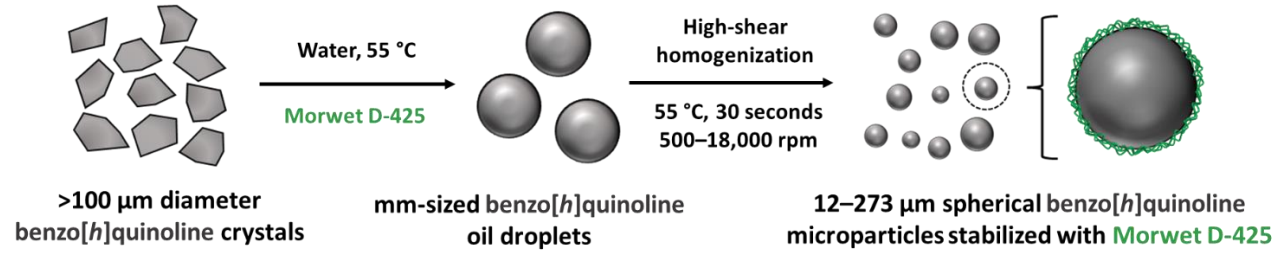

Scheme 2. Schematic cartoon for the preparation of benzo[*h*]quinoline microparticles via high-shear emulsification of molten droplets in water at 55 °C using Morwet D-425 as an emulsifier.

Effect of Emulsifier Type on Microparticle Morphology

In initial experiments, three commercial water-soluble polymers (PVA, PNVP and Morwet D-425) were evaluated for their emulsifier performance during the preparation of benzo[*h*]quinoline microparticles at a constant stirring rate of 6,000 rpm. Using PVA led to the formation of unstable microparticles with a significant fraction exhibiting a distinctive anisotropic morphology (**Figure 1a**). PNVP produced less anisotropic microparticles that proved to be unstable with respect to aggregation (**Figure 1b**). In contrast, using Morwet D-425 as an emulsifier produced polydisperse spherical microparticles of around 10-80 µm diameter (**Figure 1c**). Hence Morwet D-425 was selected for further studies.

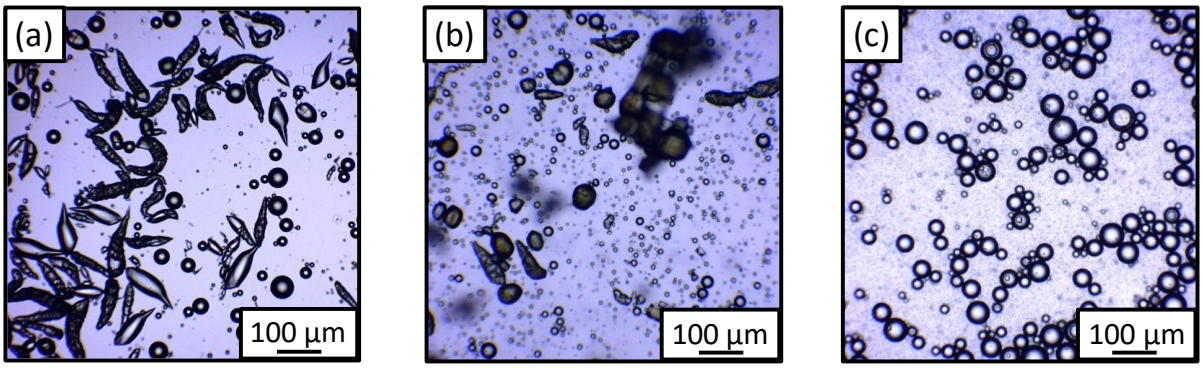

Figure 1. Representative optical microscopy images recorded for benzo[*h*]quinoline microparticles prepared via the hot emulsification route at 55 °C at a constant stirring rate of 6,000 rpm using (a) PVA, (b) PNVP or (c) Morwet D-425 emulsifier.

Effect of Stirring Rate on Microparticle Diameter

Next, the effect of stirring rate on the mean microparticle diameter was investigated when using the Morwet D-425 emulsifier (**Figure 2**). The stirring rate was adjusted from 500 rpm (magnetic stirring) to 18,000 rpm (using an Ultra-Turrax overhead stirrer). As expected, higher stirring rates led to the formation of finer oil droplets and hence smaller microparticles.

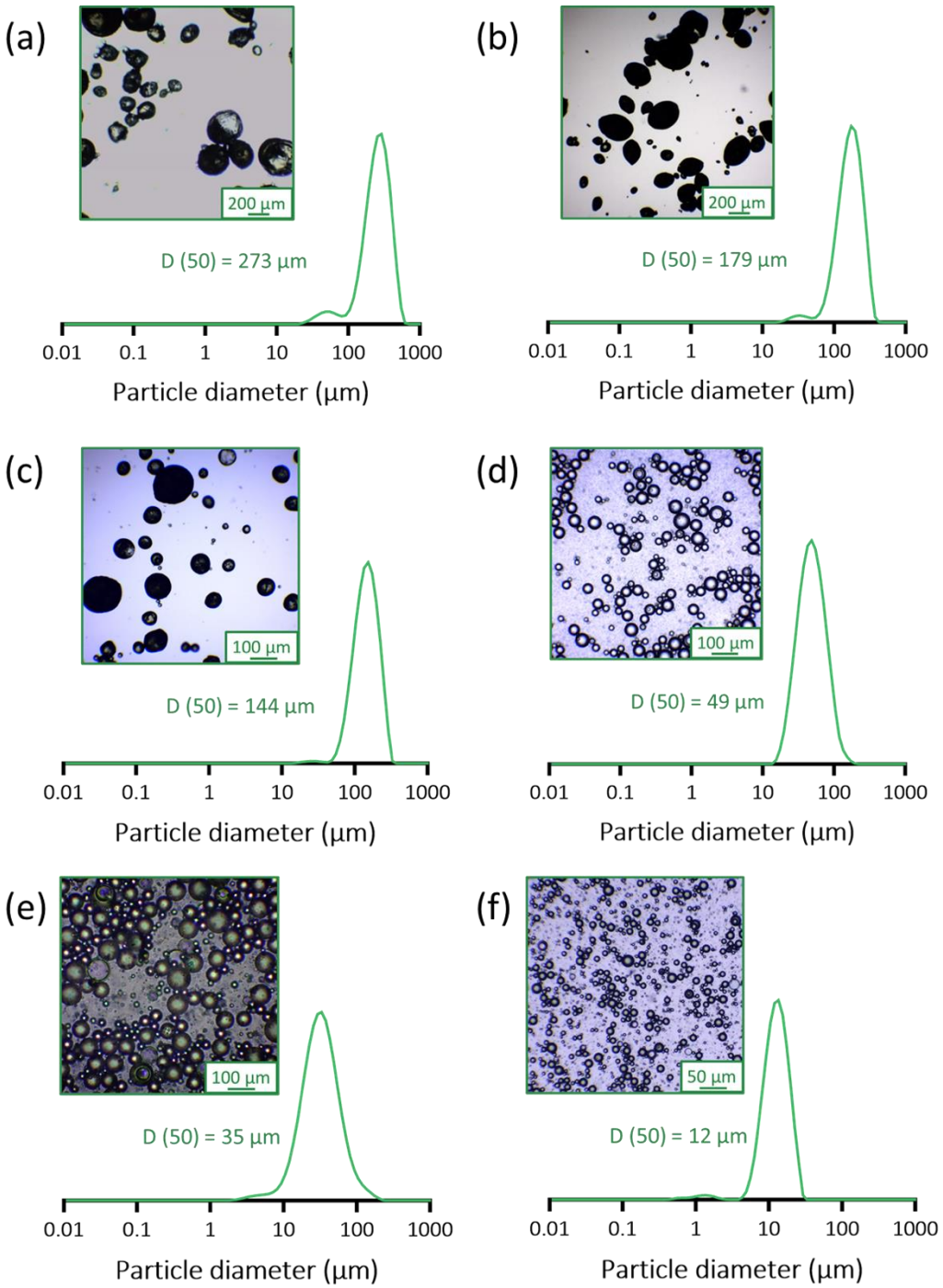

Figure 2. Laser diffraction particle size distributions and corresponding optical microscopy images recorded for benzo[*h*]quinoline microparticles prepared via the hot emulsification route using the Morwet D-425 emulsifier at 55 °C (see **Scheme 2**) using a stirring rate of (a) 500, (b) 750, (c) 3,000, (d) 6,000, (e) 12,000 or (f) 18,000 rpm.

The relationship between the mean particle diameter and the stirring rate is plotted in **Figure 3**. Similar results have been reported in the literature for various types of emulsions, including our recent phenanthrene microparticle formulation.[36,42]

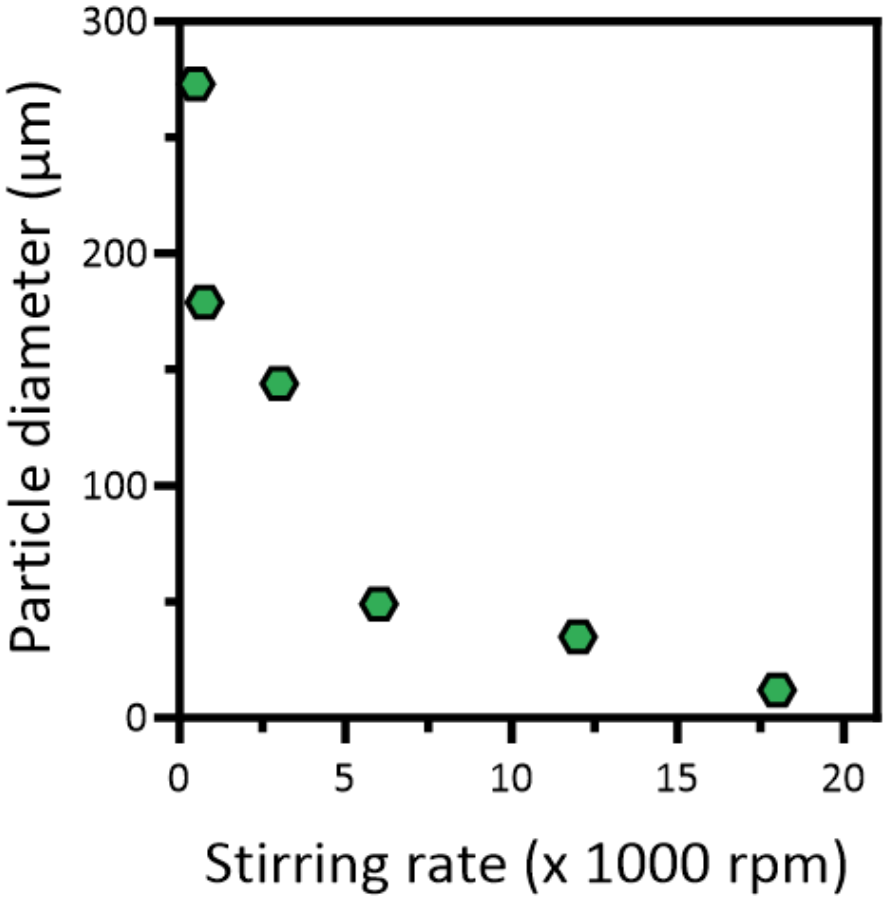

Figure 3. Effect of stirring rate on the volume-average particle diameter (D_{50}) obtained for benzo[*h*]quinoline microparticles prepared using the Morwet-D425 stabilizer emulsifier at 55°C**.**

Melting point phase diagram for a series of benzo[*h*]quinoline/phenanthrene binary mixtures

Recently, we reported the melting point phase diagram for a series of phenanthrene/pyrene binary mixtures.[41] The eutectic composition and eutectic temperature were identified and this information was used to prepare the first example of hybrid PAH microparticles. In the present study, we employ the same approach to prepare the first example of hybrid PANH/PAH microparticles. **Figure 4** shows a melting point phase diagram constructed for a series of benzo[*h*]quinoline/phenanthrene binary mixtures. Notably, the melting point of a 65:35 benzo[*h*]quinoline/phenanthrene mixture is approximately 37 °C, which is significantly lower than that of benzo[*h*]quinoline alone (51°C). This relatively low eutectic temperature is important because it enables convenient emulsification of this eutectic composition via high-shear homogenization under relatively mild conditions in aqueous solution. Moreover, working at the eutectic composition should minimize any change in composition that might occur during processing. This is a potentially important advantage in the context of the intended space science application for the target hybrid microparticles. For example, such experiments might involve the characterization of *individual* microparticles embedded within aerogel

targets using Raman microscopy,[43] hence any compositional heterogeneity between microparticles could complicate such analysis.

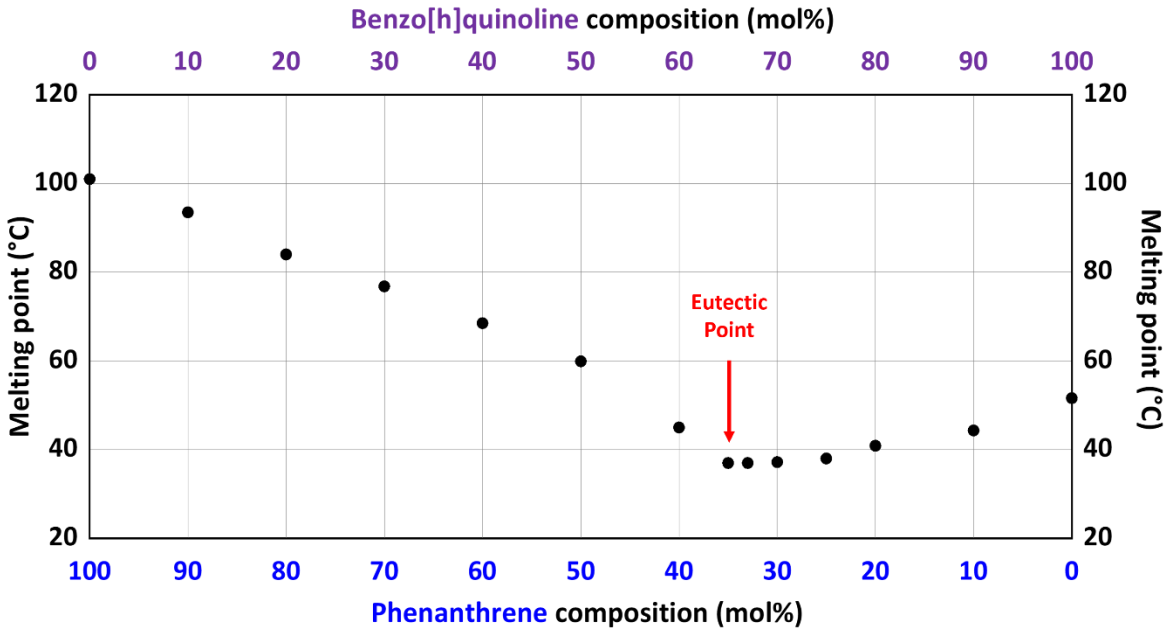

Figure 4. Melting point phase diagram constructed for a series of binary mixtures of benzo[*h*]quinoline and phenanthrene. The eutectic composition corresponds to 65 mol% benzo[*h*]quinoline and the corresponding eutectic temperature is approximately 37°C.

Synthesis and characterization of hybrid 65:35 benzo[*h*]quinoline/phenanthrene microparticles

Hybrid 65:35 benzo[*h*]quinoline/phenanthrene microparticles were prepared using the approach outlined in **Scheme 3**.

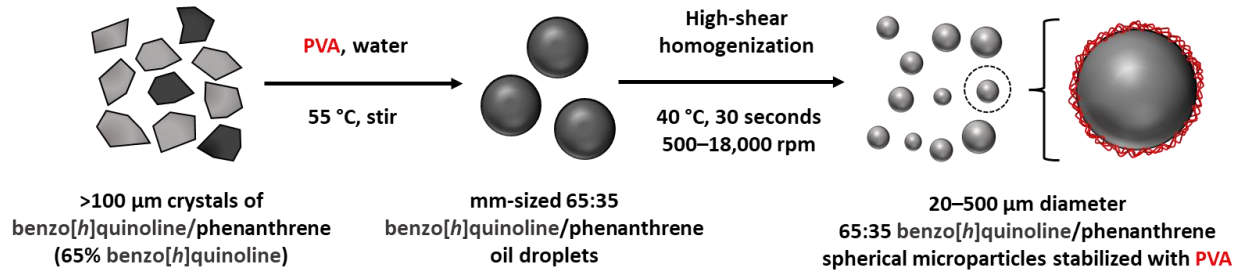

Scheme 3. Schematic cartoon for the preparation of 65:35 benzo[*h*]quinoline/phenanthrene microparticles via high-shear emulsification of molten oil droplets in water at 40 °C.

In this case, PVA was selected as an emulsifier and hot emulsification was conducted at a relatively slow stirring rate of 500 rpm at 40 °C**.** Optical microscopy studies indicated a pseudo-spherical morphology and digital image analysis using *ImageJ* software indicated a mean particle diameter of 438 ± 120 µm (**Figure 5**). Such relatively large microparticles are particularly well-suited for analysis by hot-stage optical microscopy, ^{1}H NMR spectroscopy and Raman microscopy (see below).

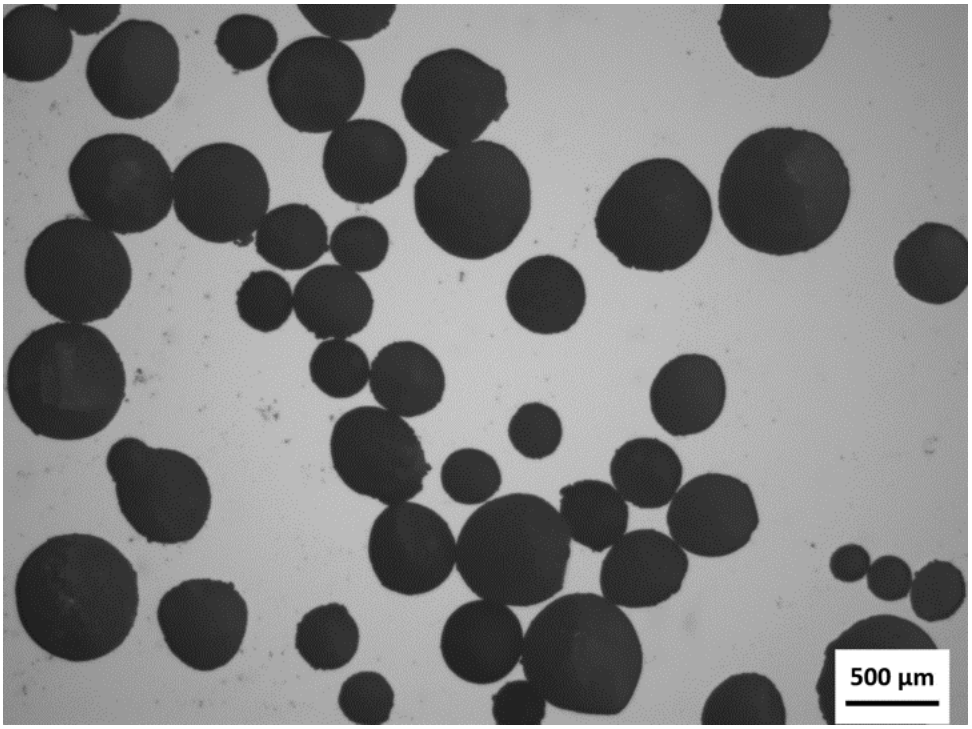

Figure 5. Optical microscopy image obtained for 65:35 benzo[*h*]quinoline/phenanthrene microparticles of 438 ± 120 µm diameter prepared via hot emulsification at 40°C using the PVA emulsifier.

As indicated above, such hybrid microparticles should ideally possess precisely the same chemical composition (i.e., 65 mol% benzo[*h*]quinoline) if they are to be used as synthetic mimics for space science applications. This is because various spectroscopic and microscopic experiments are performed on single microparticles. According to **Figure 4**, the melting point of hybrid microparticles comprising a binary mixture of benzo[*h*]quinoline and phenanthrene is sensitive to the precise composition. Thus, for sufficiently large *individual* microparticles, the compositional uniformity (or heterogeneity) can be assessed by observing their melting behavior. Accordingly, hot-stage optical microscopy was used to record images of an array of twelve 65:35 benzo[*h*]quinoline/phenanthrene microparticles (mean diameter = 438 ± 120 µm) placed on a copper sheet mounted on a Linkam temperature control unit (see **Figure S1**) during heating at 0.5°C min^{-1}. A control experiment performed using phenanthrene microparticles (mean diameter = 202 µm) confirmed that there were no unwanted thermal gradients across the copper sheet and the expected melting transitions was observed at 101°C (data not shown). Inspecting Figure 6, the array of twelve 65:35 benzo[*h*]quinoline/phenanthrene microparticles remained intact at 35°C but all microparticles underwent a melting transition at approximately 36°C, which is very close to the eutectic temperature of 37°C indicated by the melting point phase diagram (**Figure 4**). These observations suggest a high degree of chemical homogeneity for these microparticles – precisely as expected for this eutectic composition.

In addition, spectroscopic evidence was sought to confirm the constant 65 mol% benzo[*h*]quinoline composition for such hybrid microparticles. The mass of an individual benzo[*h*]quinoline/phenanthrene microparticle of 438 ± 120 µm diameter is estimated to be

approximately 50 μg, which should allow a high-quality ^{1}H NMR spectrum to be recorded. Thus, individual microparticles were dissolved in d_6-acetone (which is a good solvent for both benzo[*h*]quinoline and phenanthrene) to enable their mean composition to be determined. Ten ^{1}H NMR spectra obtained for individual benzo[*h*]quinoline/phenanthrene microparticles are shown in **Figure S2**. A typical example is shown in **Figure 7**, along with reference spectra recorded for pure benzo[*h*]quinoline and phenanthrene dissolved in d_6-acetone. The benzo[*h*]quinoline/phenanthrene molar ratio was determined in each case by comparing the integrated blue signal assigned to the proton adjacent to the nitrogen atom in benzo[*h*]quinoline (**Figure 7b**) to the red signals corresponding to the two C-H protons within the 'bay' of the phenanthrene molecule (**Figure 7a**). Such microparticles are expected to contain 65 mol% benzo[*h*]quinoline, so the integrated signal ratio should be 0.93. Averaging over ten microparticles, the experimental ratio was calculated to be 0.92 ± 0.01. Thus these hybrid microparticles clearly possess the desired chemical composition within experimental error. In principle, similar hot-stage optical microscopy and NMR experiments could be performed for smaller microparticles. In practice, the precise manipulation of, say, 100 μm diameter microparticles to form a suitable array for the former technique becomes extremely challenging, while only poor-quality NMR spectra could be obtained for similar-sized microparticles (mass scales as the cube of the radius, so microparticles of 100 μm diameter possess a mass of less than 1 μg).

Raman microscopy was used to assess the chemical composition of *individual* hybrid microparticles (**Figure 8**). The Raman spectra recorded for phenanthrene and benzo[*h*]quinoline contain many common bands (e.g., at ~409, 549, 709 cm^{-1}) corresponding to various in-plane skeletal vibrations of the aromatic ring structure. However, unique bands for phenanthrene are observed at 828, 1244, 1349 and 1522 cm^{-1} while bands at 843, 1343 and 1401 cm^{-1} are exhibited solely by benzo[*h*]quinoline. In particular, the 828 and 843 cm^{-1} bands correspond to equivalent in-plane ring stretching modes for these two aromatic molecules, with the 15 cm^{-1} difference resulting from more asymmetric stretching of benzo[*h*]quinoline (owing to its pyridine ring). The phenanthrene bands observed at 1244, 1349 and 1522 cm^{-1} are assigned to C-H wagging modes. The benzo[*h*]quinoline band at 1343 cm^{-1} corresponds to a strong wagging motion for the C-H bond closest to the pyridine nitrogen, coupled to a C-C ring stretch primarily associated with the benzene ring furthest from the pyridine unit (with no equivalent vibrational mode for phenanthrene). Similarly, the benzo[*h*]quinoline band at 1401 cm^{-1} is assigned to the wagging motion of the C-H bond opposite the pyridine nitrogen coupled to a ring stretch primarily associated with the central benzene ring. Importantly, **Figure 8** confirms that individual microparticles contain both benzo[*h*]quinoline and phenanthrene, with a significantly higher proportion of the former molecule. Thus these Raman spectra are consistent with the expected eutectic composition of 65:35 benzo[*h*]quinoline/phenanthrene.

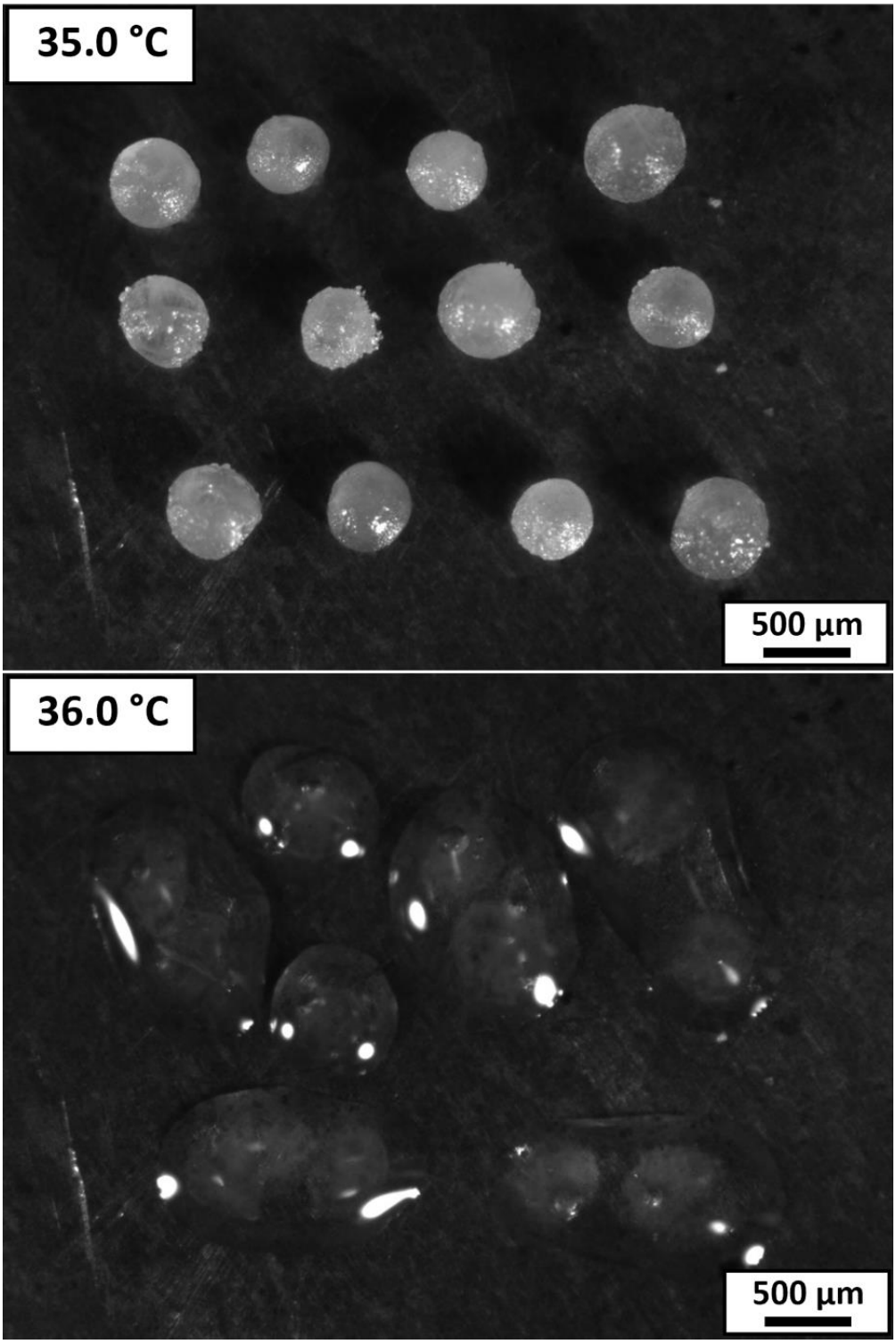

Figure 6. Representative images recorded during hot-stage optical microscopy studies of an array of twelve 65:35 benzo[*h*]quinoline/phenanthrene microparticles of 438 ± 120 µm diameter. The heating rate used in this experiment was 0.5°C min^{-1}. The microparticles remain intact up to 35°C and begin to melt at 36°C. This behavior is consistent with the eutectic temperature of approximately 37°C indicated in **Figure 4**.

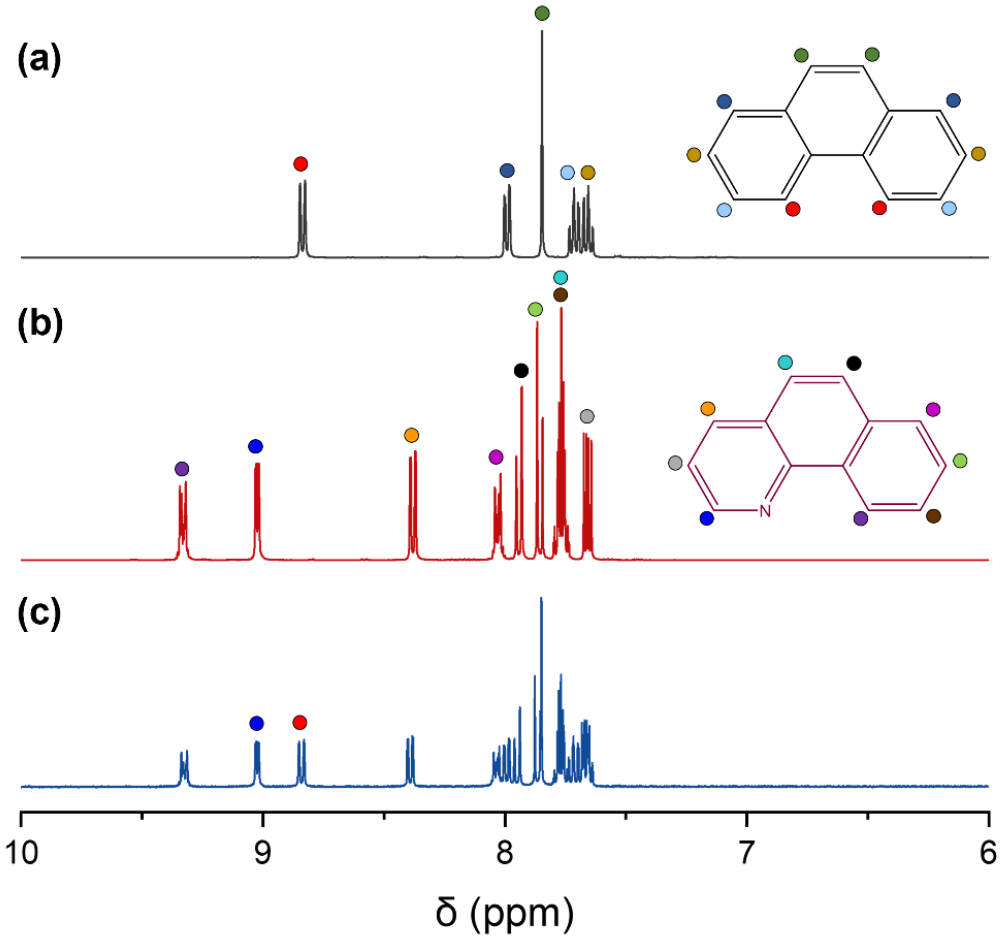

Figure 7. Assigned ^{1}H NMR spectra (d_6-acetone, 400 MHz) recorded for (a) phenanthrene, (b) benzo[*h*]quinoline and (c) an individual 65:35 benzo[*h*]quinoline/phenanthrene microparticle (mean diameter = 438 ± 120 μm).

It is well-known that polycyclic aromatic hydrocarbons such as phenanthrene exhibit autofluorescence.[36,44–47] Indeed, this intrinsic property has been exploited by environmental scientists to monitor the presence of such molecules – which are regarded as persistent toxic pollutants – within plants and soil.[44–47] Recently, we reported that the autofluorescence exhibited by phenanthrene (and pyrene) aids the analysis of craters formed after firing such microparticles into a metal target using a light gas gun.[36] In view of this prior study, we examined 65:35 benzo[*h*]quinoline/phenanthrene microparticles of 438 ± 120 μm diameter using fluorescence microscopy (see **Figure 9**). An image of such microparticles recorded using conventional optical microscopy is shown in **Figure 9a**. Switching to fluorescence mode, the microparticles clearly exhibit autofluorescence (see **Figures 9b** and **9c**). Significantly stronger emission is observed when selecting longer excitation/emission wavelengths. Some of the microparticles appear to be porous (see small dark patches in **Figure 9c**); on the other hand, such features might simply be surface defects. In contrast, much weaker fluorescence is observed for the purely benzo[*h*]quinoline microparticles (see **Figure S3**).

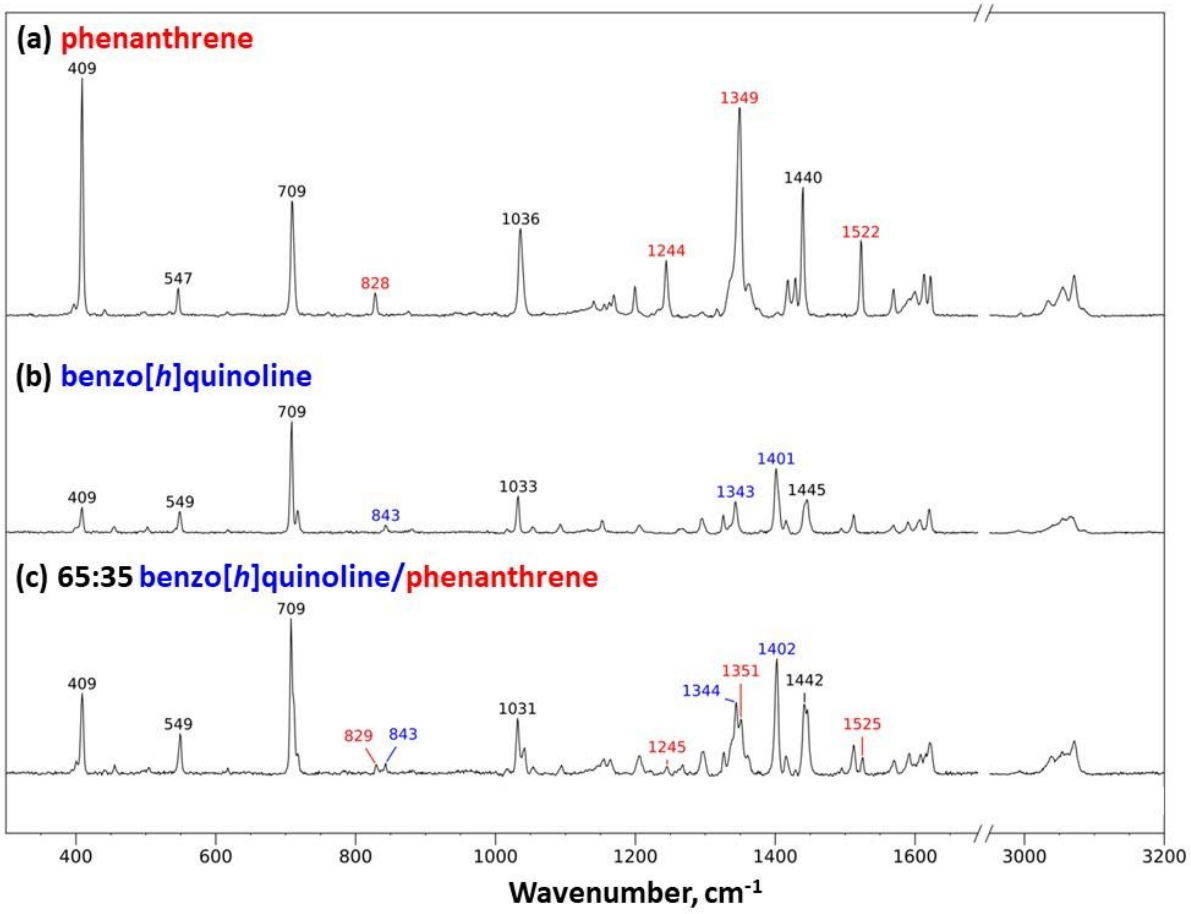

Figure 8. Representative spectra recorded for *individual* microparticles using Raman microscopy: (a) phenanthrene, (b) benzo[*h*]quinoline and (c) 65:35 benzo[*h*]quinoline/phenanthrene.

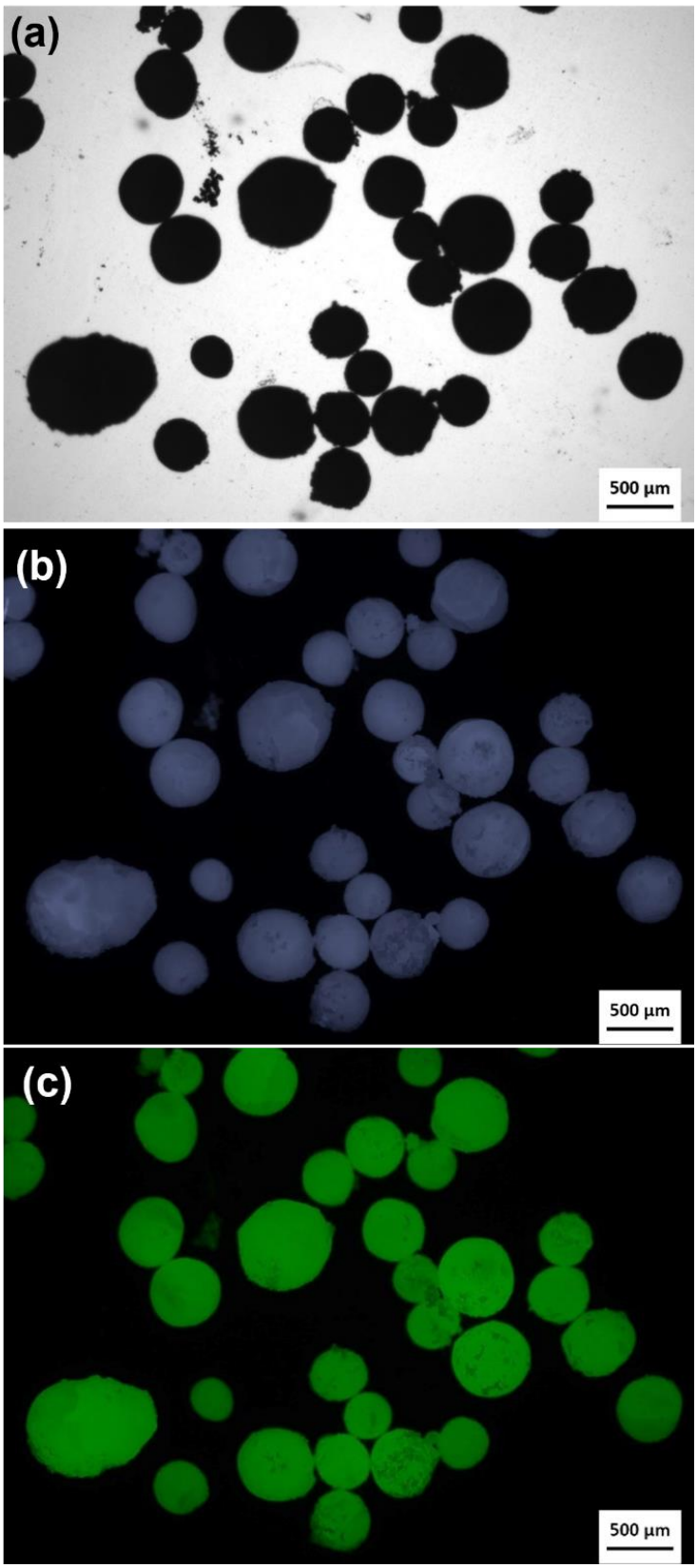

Figure 9. Representative images recorded for 65:35 benzo[*h*]quinoline/phenanthrene microparticles of 438 ± 120 µm diameter: (a) optical micrograph, (b) fluorescence micrograph (filter set 02; excitation λ = 365 nm; emission λ > 420 nm) and (c) fluorescence micrograph (filter set 38; excitation λ = 470 nm; emission λ = 525 nm).

Synthesis of 65:35 benzo[h]quinoline/phenanthrene microparticles of 20 to 120 µm diameter

Heating a 65:35 benzo[*h*]quinoline/phenanthrene binary mixture at 55 °C initially produced millimeter-sized molten droplets. Subsequent high-shear homogenization at 40 °C in the presence of the PVA emulsifier produced much finer droplets (see **Figure 10**). Systematic variation of the stirring rate provided control over the mean droplet diameter, as expected (see **Figure 11**).

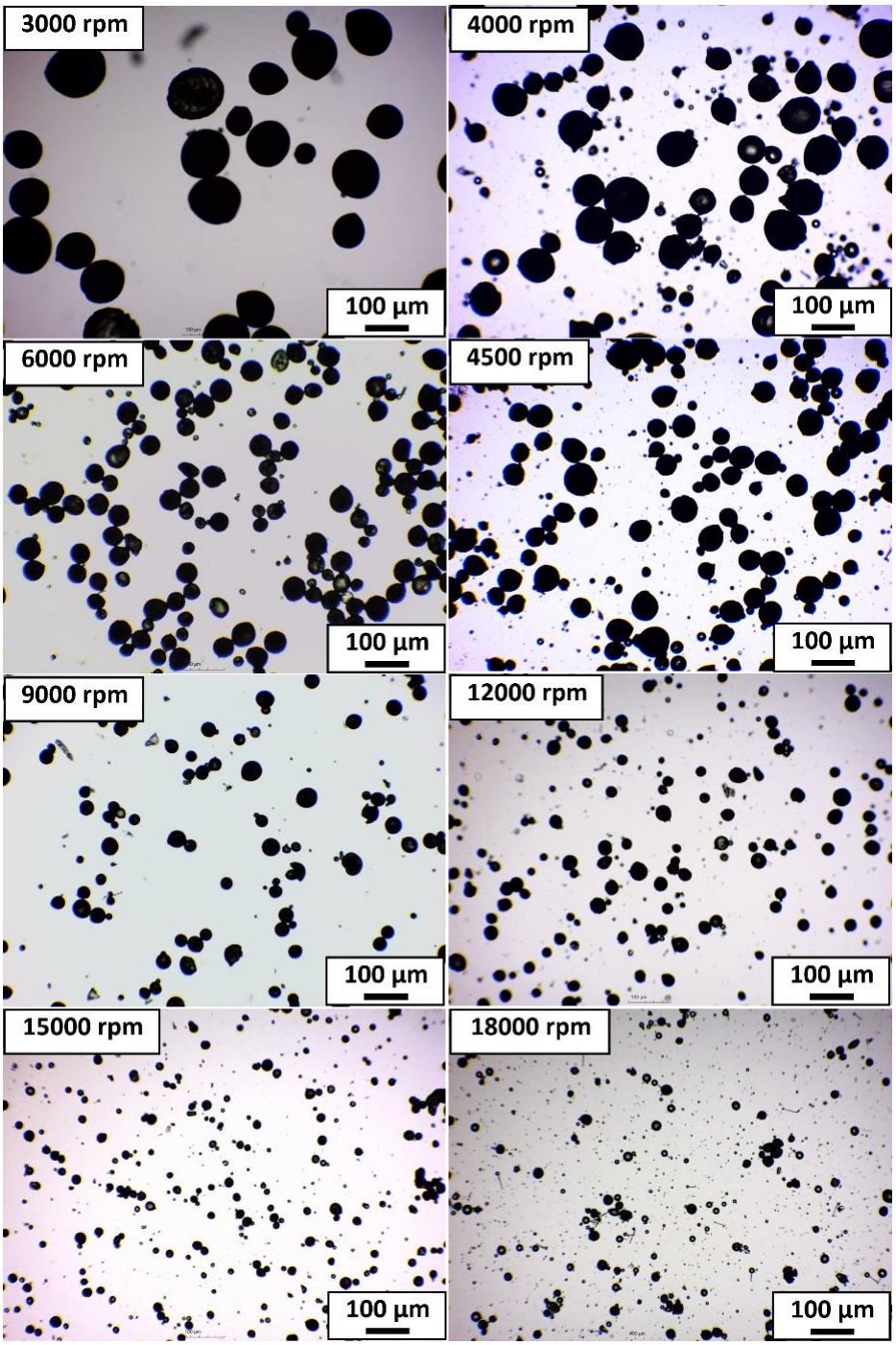

Figure 10. Representative optical microscopy images recorded for a series of 65:35 benzo[*h*]quinoline/phenanthrene microparticles prepared via hot emulsification at 40°C using the PVA emulsifier. Systematically increasing the stirring rate from 3,000 rpm to 18,000 rpm leads to progressively smaller microparticles.

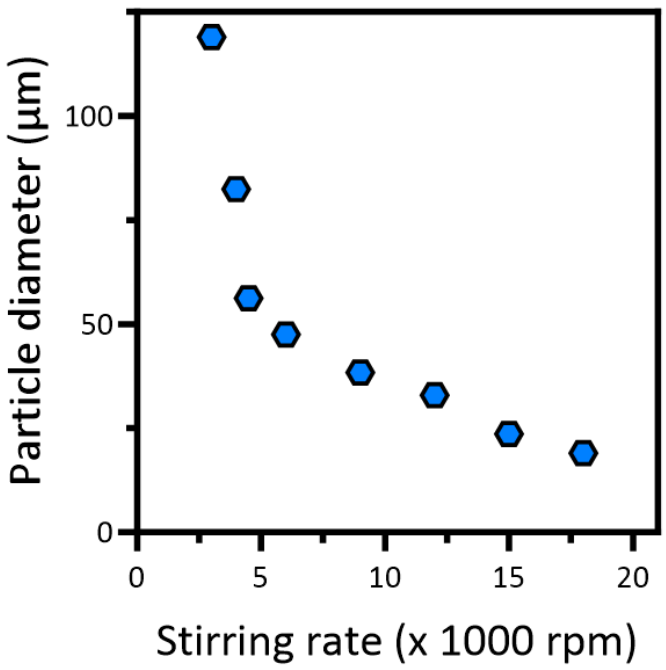

Figure 11. Effect of varying the stirring rate on the volume-average particle diameter (D_{50}) for 65:35 benzo[*h*]quinoline/phenanthrene microparticles prepared via hot emulsification at 40°C using the PVA emulsifier.

Recrystallization of the dispersed phase occurred on cooling to produce spherical 65:35 benzo[*h*]quinoline/phenanthrene microparticles of approximately 20 to 120 µm diameter, as judged by laser diffraction studies (see **Figure 12**).

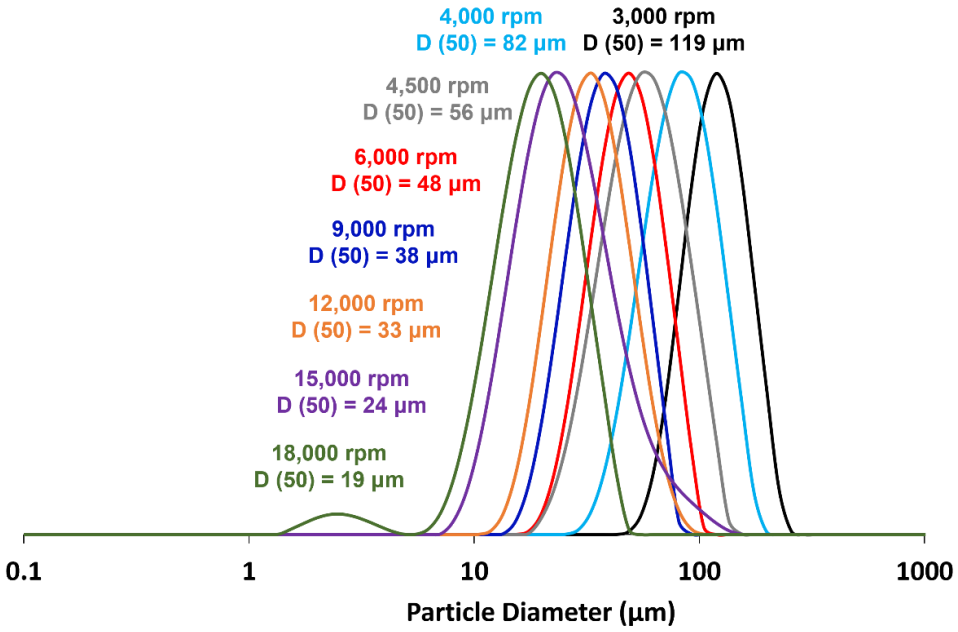

Figure 12. Laser diffraction particle size distributions recorded for a series of 65:35 benzo[*h*]quinoline/phenanthrene microparticles prepared via hot emulsification at 40°C using the PVA emulsifier.

A unimodal size distribution was observed for each formulation, except for the microparticles prepared at the highest stirring rate of 18,000 rpm (green curve). In this case, a minor population of smaller microparticles of approximately 2-6 μm diameter was also present.

Light Gas Gun Experiments

Details of the four impact experiments plus a control shot conducted using the Light Gas Gun facility at the University of Kent[34,40] are summarized in **Table 1**.

Table 1. Summary of impact experiments conducted using the new PANH-based microparticles reported in this study.

Projectile composition	**Microparticle diameter (μm)**	**Target**	**Speed (km s^{-1})**
Benzo[*h*]quinoline	35	Aluminum foil	0.87 ± 0.03
Benzo[*h*]quinoline	273	SIlica aerogel	0.98 ± 0.04
65:35 benzo[*h*]quinoline/phenanthrene	65	Aluminum foil	0.90 ± 0.04
65:35 benzo[*h*]quinoline/phenanthrene	65	SIlica aerogel	1.01 ± 0.04
Empty sabot containing no microparticles	Not applicable	Aluminum foil	1.01 ± 0.04

The control shot using an empty sabot containing no microparticles produced some carbon-rich clusters on the aluminum foil target. Such artifacts arise from various types of gun debris. When similar features were observed in experiments performed using the two types of PANH microparticles reported in **Table 1**, they were excluded from further analysis. No surface indentations[48] were observed on the aluminum target for this control shot but such features were observed when firing the PANH microparticles at 0.87-0.90 km s^{-1}. Typical impact features on the aluminum foil are shown in Figure 13a and 13c when using the 35 μm benzo[*h*]quinoline microparticles and in **Figure 13e** when using the 65 μm 65:35 benzo[*h*]quinoline/phenanthrene microparticles. In both cases, the impinging microparticles rebound at this comparatively low impact speed: only relatively shallow indentations of 12 to 37 μm diameter are observed, with no signs of deeper impact craters with raised rims. Analytical X-ray elemental mapping confirms the presence of carbonaceous debris around the edges of the indentations formed by the 35 μm benzo[*h*]quinoline microparticles (**Figure 12b** and **12d**) but there is minimal evidence for similar debris originating from the 65 μm 65:35 benzo[h]quinoline/phenanthrene microparticles (**Figure 13f**). Unfortunately, no characteristic Raman spectra could be recorded from such impact features, while UV illumination of the target area indicated no observable fluorescence. Hence there is minimal transfer of mass from the impinging microparticles to the aluminum foil target.

Similar rebound behavior has been reported for various types of projectiles fired at aluminum foil at comparable speeds.[28,49,50] For example, 4 - 10 μm diameter poly(methyl methacrylate) microparticles fired at 0.8 to 1.0 km s^{-1} also rebound off the target surface.[49] Of particular relevance to the present study, anthracene microparticles fired into aluminum foil at 1.87 km s^{-1} also produced relatively shallow craters with relatively low levels of carbonaceous debris.[33]

In contrast, 279 μm diameter 75:25 phenanthrene/pyrene microparticles fired into aluminum foils at 0.96 km s^{-1} resulted in extensive projectile fragmentation, with significant retention of carbonaceous debris at the impact site.[41] Similarly, 75 – 90 μm diameter salt grains produce slightly more pronounced impact craters/indentations when fired into aluminum foil at 0.5 – 1.0 km s^{-1}. In this case, the mass of projectile residues associated with the impact craters was sufficient to allow both X-ray elemental mapping and Raman microscopy studies, particularly at higher impact speeds.[51] Finally, well-defined craters with substantial carbonaceous deposits on the crater floor were observed when firing phenanthrene microparticles into aluminum foil at 1.87 km s^{-1}.[36]

For a given target, the extent of crater formation depends on (i) the size and type of projectile and (ii) the impact speed. Traditionally, the shock pressure generated during the impact is also a critical parameter. This can be estimated using the planar impact approximation (PIA).[52] This requires the target and projectile densities, plus separate linear shock wave speed relations for both target and impactor. The wave speed relations are of the form U = C + S.u, where U is the shock wave speed, u is the particle speed, and C and S are the relevant shock Hugoniot coefficients for a given material. Unfortunately, we have been unable to find any shock wave data for benzo[*h*]quinoline (ρ = 1241 kg m^{-3}) in the literature. As an approximation, we use shock wave data for a similar compound (anthracene) with a comparable density (ρ = 1249 kg m^{-3}). The C and S values summarized in **Table 2** were obtained by a fit to literature data.[53] Hence we calculate that 35 μm diameter benzo[*h*]quinoline microparticles fired into aluminum foil at 0.87 km s^{-1} produce a shock peak pressure of 3.45 GPa.

Similarly, we were unable to find shock Hugoniot coefficients in the literature for 65:35 benzo[h]quinoline/phenanthrene hybrid microparticles. Accordingly, we estimated a likely range for the peak shock pressure using literature data for phenanthrene and anthracene (as a proxy for benzo[*h*]quinoline). Thus, for an impact of 65:35 benzo[h]quinoline/phenanthrene hybrid microparticles on aluminum foil at 0.90 km s^{-1}, the estimated peak shock pressure lies between 2.89 GPa (for phenanthrene) and 3.57 GPa (for benzo[*h*]quinoline).

Table 2. Summary of material densities and shock Hugoniot coefficients used to calculate peak shock pressures using the Planar Impact Approximation.

Material	**C (km s^{-1})**	**S**	**Density (kg m^{-3})**	**Source**
Anthracene	1.109	3.540	1249	Ref[53]
Phenanthrene	3.139	0.309	1212	Ref[36]
Aluminum	5.376	1.339	2712	Ref[53]
Silica aerogel	0.2825	2.629	89	Ref[54]

In our previous study,[41] the peak shock pressure was estimated to lie between 3.12 GPa and 3.75 GPa when firing 279 μm 75:25 phenanthrene/pyrene microparticles into aluminum foil at 0.96 km s^{-1}. The peak shock pressure of 3.45 GPa calculated above falls within this range, suggesting comparable impact shock conditions. The observed differences in impact crater formation must therefore reflect some other property of the impinging microparticles (e.g., their compressive strength, melting point, etc.), which govern projectile fracture and deposition of projectile debris.

The peak post-shock temperature (T_{pps}) within the most heavily shocked part of an impinging projectile can also be estimated.[55,56] This is the maximum temperature of the decompressed shocked material arising from heat generated after shock and release and is given by:

$$T_{pps} = T_0 + [(u^2 - 2E_r)/2C_p] \quad (1)$$

where C_P is the specific heat capacity, T_0 is the ambient temperature, E_r is the energy lost from the projectile during decompression from its shocked state. E_R is given by:

$$E_R = (C/S)*[u + (C/S)*\ln(C/U)] \quad (2)$$

where C and S are the shock Hugoniot coefficients for the impinging projectile mentioned above and u and U are the appropriate values of the particle speed and shock wave speed respectively at the peak shock pressure. This approach has been used to analyze high-speed impacts on aluminum foil for several types of microparticles, including salt[51] and phenanthrene.[36] Taking C_p = 206.36 J mol^{-1} K^{-1} for benzo[*h*]quinoline,[57] an ambient temperature of 293 K, and the E_R value calculated using the C and S values for anthracene as a proxy for benzo[*h*]quinoline (see above), then T_{pps} is estimated to be 41 °C for an impact speed of 0.87 km s^{-1}. Importantly, this maximum post-shot temperature is below the melting point of benzo[h]quinoline (51°C). This suggests that the impinging benzo[h]quinoline microparticles are unlikely to melt during such a high-speed impact, which is consistent with the minimal carbonaceous residues detected within the shallow indentations show in **Figure 13**.

The calculation of peak post-shock temperatures via equation (1) for high-speed impacts produced by impinging hybrid benzo[*h*]quinoline/phenanthrene microparticles are somewhat problematic owing to the lack of relevant shock wave data. Nevertheless, a range of temperatures can be calculated for projectiles comprising either benzo[*h*]quinoline (approximated using anthracene literature data) or phenanthrene (taking C_p = 220.62 J mol^{-1} K^{-1} for phenanthrene).[58] At an impact speed of 0.90 km s^{-1}, T_{pps} ranges between 30 °C (for phenanthrene) and 43 °C (for benzo[*h*]quinoline). Given that the eutectic melting point of 37 °C for the 65:35 benzo[h]quinoline/phenanthrene hybrid microparticles falls within this range, at least part of the most heavily shocked front face of such projectiles may begin to melt when striking the aluminum foil target. However, there is no significant evidence for such partial melting within the impact features. In this case, more accurate shock Hugoniot coefficients for both the benzo[*h*]quinoline and the 65:35 benzo[h]quinoline/phenanthrene hybrid microparticles are clearly required.

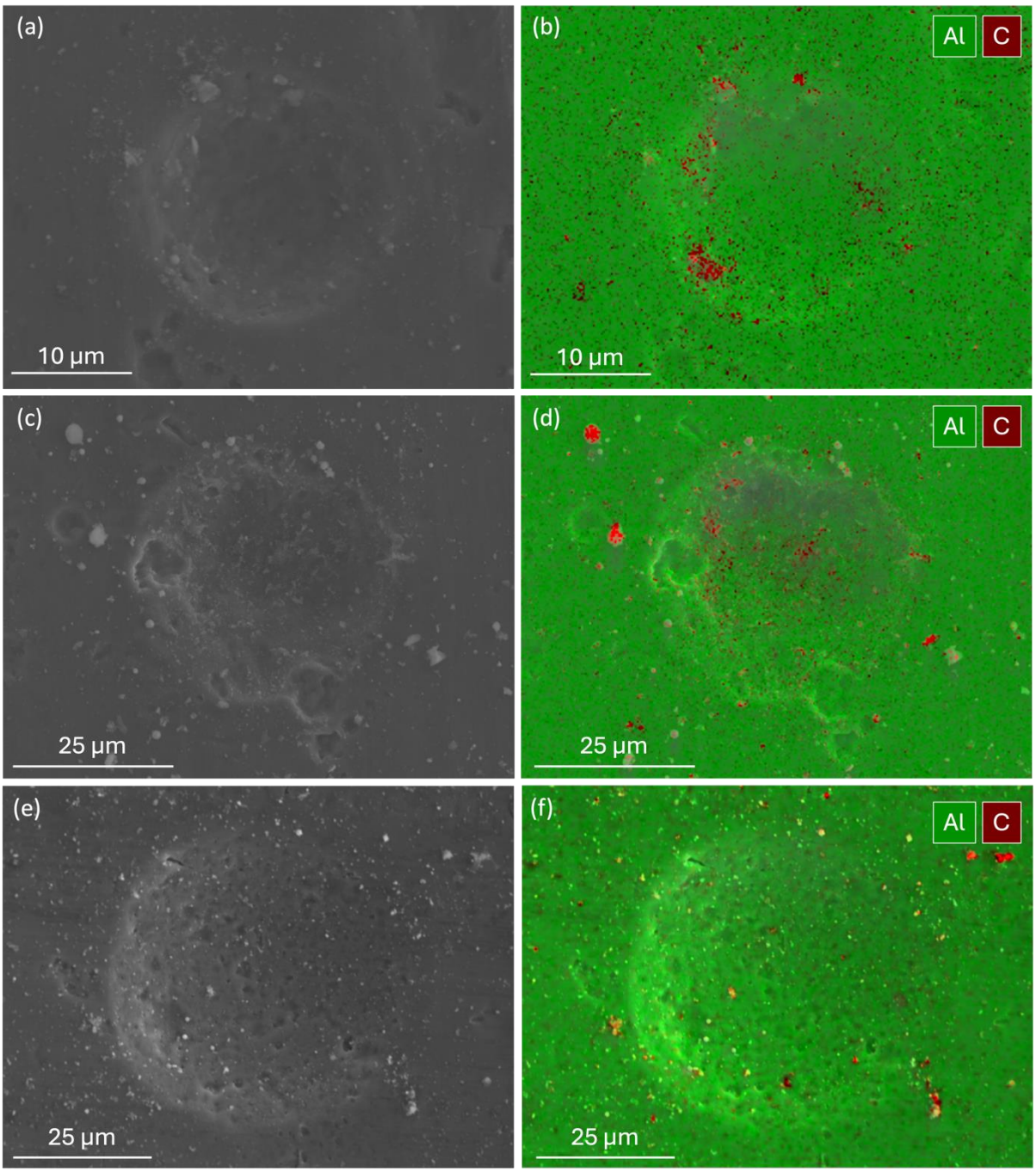

Figure 13. Representative SEM images recorded for shallow indentations of (a) ~19 µm diameter and (c) ~36 µm diameter observed after firing 35 µm diameter benzo[*h*]quinoline microparticles into an aluminum foil target at 0.87 km s^{-1}. (b, d) Corresponding analytical X-ray elemental maps (green denotes aluminum and red denotes carbon) recorded for the impact features shown in (a) and (c), respectively. (e) SEM image recorded for a ~52 µm indentation produced after firing 65 µm diameter 65:35 benzo[*h*]quinoline/phenanthrene microparticles into an aluminum foil target at 0.90 km s^{-1}. (f) The corresponding analytical X-ray elemental map (green denotes aluminum and red denotes carbon) shows little sign of carbonaceous deposits associated with this impact feature in this case.

When benzo[*h*]quinoline microparticles of 273 µm diameter were fired at 0.981 km s^{-1} into a silica aerogel target (ρ = 89.3 kg m^{-3}), optical microscopy studies indicated the formation of distinctive tracks within the aerogel, see **Figure 14a**. These tracks are relatively long and tapered; hence they

are often described as carrot tracks in the aerogel capture literature.[27,59] The carrot tracks here range from ~ 5 mm to ~ 7 mm in length (i.e. up to 26 times longer than the mean diameter of the original impinging microparticles). Recently, we reported[41] the formation of similar carrot tracks during the capture of 75:25 phenanthrene/pyrene hybrid microparticles fired at 1 km s^{-1} into a silica aerogel target of comparable density (ρ = 91.5 kg m^{-3}).

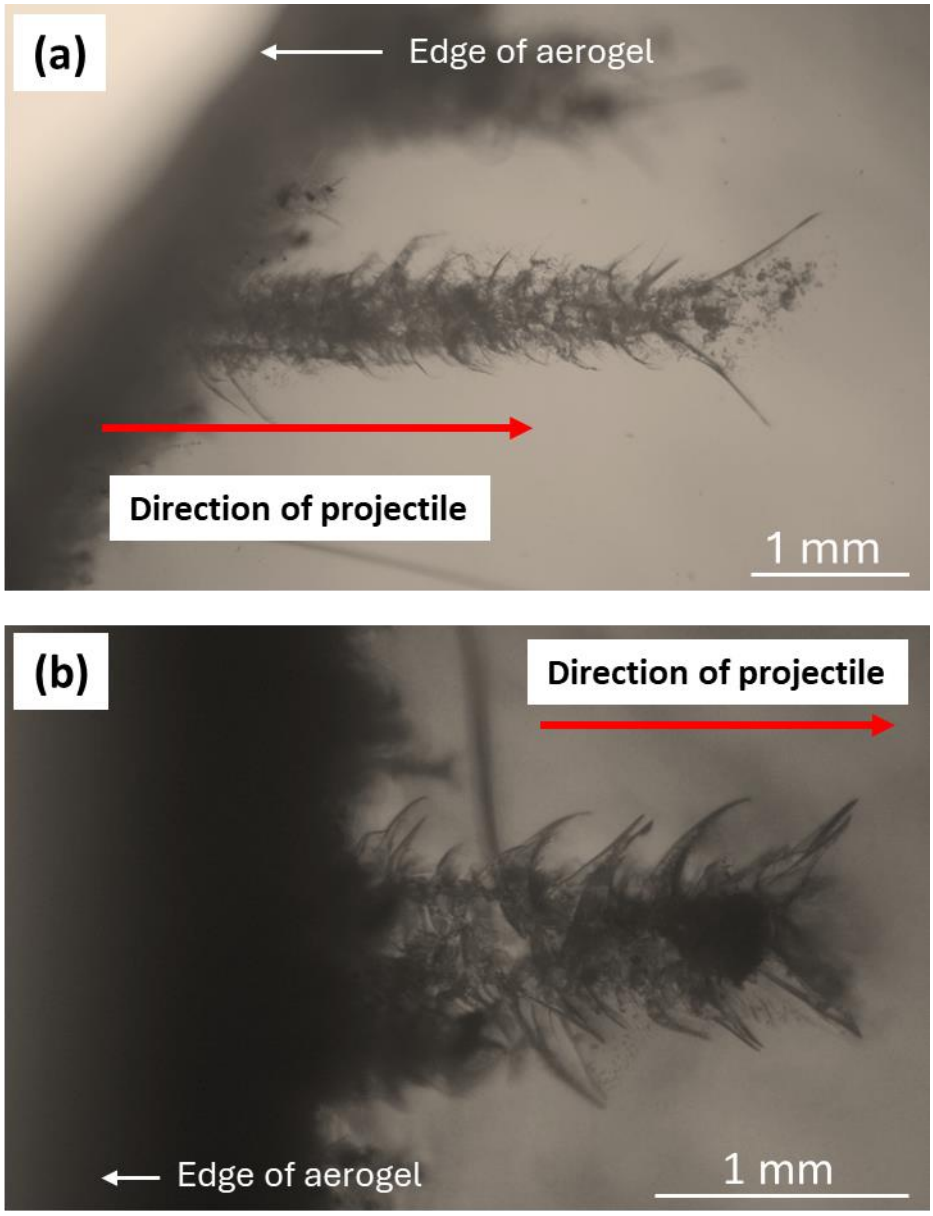

Figure 14. (a) Optical microscopy side-view image recorded after firing 273 μm diameter benzo[*h*]quinoline microparticles at 0.98 km s^{-1} into a silica aerogel target (ρ = 89 kg m^{-3}). The projectiles were travelling left to right. Particle debris (dark material) can be identified both along and (in some cases) at the end of the carrot tracks. (b) Optical microscopy image (side-view) recorded after firing 65:35 benzo[*h*]quinoline/ phenanthrene microparticles of 65 μm diameter at 1.01 km s^{-1} into a silica aerogel target (ρ = 89 kg m^{-3}).

Discrete microparticles were observed at the end of a few carrot tracks (**Figure 14a**). Some material was also deposited along the track walls, presumably owing to thermal ablation of the impinging microparticles. In our prior study[41] of 75:25 phenanthrene/pyrene hybrid microparticles striking a silica aerogel target at 1 km s^{-1}, UV illumination enabled partially ablated microparticles to be identified at the ends of carrot tracks, with some fragments also deposited along the tracks. Unfortunately, the benzo[*h*]quinoline microparticles employed in the present study do not exhibit autofluorescence. Nevertheless, optical microscopy studies suggest a higher degree of thermal ablation for these lower melting point microparticles.

Similar thermal ablation has been reported for model 20 µm diameter polystyrene microparticles striking a silica aerogel target (ρ = 35 kg m^{-3}).[43] In this prior study, the microparticles were captured intact at the end of their carrot tracks when fired at 2 km s^{-1}, suggesting negligible thermal ablation. However, a significant reduction in particle size was observed at 3 km s^{-1}. Such observations are consistent with the capture of phenanthrene microparticles fired into a silica aerogel target (ρ = 35 kg m^{-3}) at 2 km s^{-1}, which causes some degree of surface ablation.[36] For the benzo[*h*]quinoline experiments reported herein, the slightly denser aerogel is likely to induce ablation at a lower impact speed. Moreover, such low melting point microparticles should be more susceptible to thermal ablation. In the future, we plan to perform experiments using a series of PANH/PAH microparticles exhibiting a range of melting points and aerogel targets of variable density.

Using coefficients from **Table 2** and assuming that benzo[*h*]quinoline behaves like anthracene, the peak shock pressure calculated using the PIA for benzo[*h*]quinoline microparticles fired into a silica aerogel target at 0.981 km s^{-1} is approximately 0.21 GPa. As expected, this is significantly lower than that calculated for impacts on aluminum foil owing to the highly porous nature of the aerogel. As the microparticle tunnels into the aerogel, it experiences thermal heating. Under such conditions, the method outlined above for the calculation of the peak post-shock temperature is no longer applicable. Instead, we assume that a fraction, *f*, of the original kinetic energy heats up each microparticle as it tunnels into the aerogel target. Our prior study of the thermal ablation of 20 µm polystyrene microparticles suggest a minimum *f* value of 0.35.[43] Given the impact speed selected herein and the specific heat capacity of benzo[*h*]quinoline, this suggests that the microparticles should experience an increase in temperature of 150 °C, albeit for a short time. Given the relatively low melting point of benzo[*h*]quinoline, this explains why the ends of many carrot tracks contain no microparticles. Thus the example shown in **Figure 14a** most likely results from a significantly larger impinging microparticle.

The 65:35 benzo[*h*]quinoline/phenanthrene microparticles were fired into a silica aerogel target at 1.01 km s^{-1}. Optical microscopy studies revealed multiple characteristic carrot tracks, which are much longer than the original mean microparticle diameter of 65 µm (see **Figure 14b**). At the end of these tracks, fan-like fractures are observed within the aerogel; such features have been reported for prior aerogel capture experiments.[59,60] These carrot tracks are notably shorter than those observed for the pure benzo[*h*]quinoline microparticles of 273 µm diameter. This is simply because the latter microparticles possess much higher kinetic energy at a given impact speed owing to their significantly higher mass. Furthermore, such short tracks are significantly wider (relative to their length) compared to the long thin carrot tracks shown in **Figure 14a**. Similar observations were reported by Burchell et al. when conducting a series of aerogel calibration experiments using model

inorganic projectiles.[27] Importantly, no residual microparticles were observed at the ends of any of these carrot tracks. This suggests a high degree of ablation, which is consistent with the relatively low melting point of such microparticles.

Conclusions

The melting point of benzo[*h*]quinoline, is relatively low (ca. 51°C), which facilitates its hot emulsification under high shear at 55°C to produce the first example of well-defined spherical microparticles of adjustable diameter comprising a *heteroatom* polycyclic aromatic hydrocarbon. Moreover, blending this compound with phenanthrene in varying proportions enables the construction of a melting point phase diagram for such binary mixtures. A eutectic composition is obtained at approximately 65 mol% benzo[*h*]quinoline, which exhibits a corresponding melting point of just 37°C. This enables convenient hot emulsification processing to be conducted at 40°C.

The effect of systematically varying the stirring rate and emulsifier type is studied for both pure benzo[*h*]quinoline and the eutectic composition of 65:35 benzo[*h*]quinoline/phenanthrene. Empirically, we find that Morwet D-425 is preferred as an emulsifier for the preparation of benzo[*h*]quinoline microparticles, whereas PVA is the best choice for producing 65:35 benzo[*h*]quinoline/phenanthrene hybrid microparticles. In each case, a polydisperse spherical morphology can be obtained. As expected, the mean microparticle diameter can be readily adjusted from 273 µm at 500 rpm to 12 µm at 18,000 rpm for the benzo[*h*]quinoline microparticles and from 19 µm at 18,000 rpm to 119 µm at 3,000 rpm for the 65:35 benzo[*h*]quinoline/phenanthrene hybrid microparticles. The latter microparticles exhibit autofluorescence, which may prove to be useful for impact crater analysis and/or aerogel capture experiments. Moreover, both hot-stage optical microscopy and ^{1}H NMR spectroscopy studies suggest minimal compositional heterogeneity, i.e., there is little or no variation in the eutectic composition between microparticles. Such microparticles comprise the first examples of model synthetic mimics[61] for *heteroatom* polycyclic aromatic hydrocarbon-based cosmic dust.

In preliminary light gas gun experiments, selected microparticles have been fired at both aluminum foil and aerogel targets at around 1 km s^{-1}. The microparticles simply rebound from the former target: there is no evidence for either crater formation or microparticle fragmentation/melting. In contrast, attempted capture within an aerogel target leads to complete thermal ablation of the microparticles, which is ascribed to their relatively low melting points. Such experiments indicate that the impact outcome is strongly dependent on the nature of both the impinging projectile and the type of target. Systematic studies over a wider range of impact speeds, including those likely to be encountered in space mission dust collection scenarios, are now required to understand the various biases that arise when attempting to analyze and collect PANH cosmic dust using unmanned spacecraft in the future.

Supporting Information. Chemical structures of the three polymeric emulsifiers evaluated in this study; hot-stage optical reflectance microscopy experimental set-up; ^{1}H NMR spectra for ten 65:35 benzo[*h*]quinoline/phenanthrene microparticles; optical/fluorescence images recorded for benzo[*h*]quinoline microparticles.

Acknowledgements. The Leverhulme Trust is thanked for postdoctoral support for Dr. D. H. H. Chan (RPG-2022-260). STFC is acknowledged for funding a PhD studentship for J. L. W.

References

(1) Allamandola, L. J.; Tielens, A. G. G. M.; Barker, J. R. Polycyclic Aromatic Hydrocarbons and the Unidentified Infrared Emission Bands: Auto Exhaust along the Milky Way. *Astrophys. J.* **1985**, *290*, L25–L28.

(2) Allamandola, L.J., Tielens, A.G.G.M. Barker, J. R. Interstellar Polycyclic Aromatic Hydrocarbons: The Infrared Emission Bands, The Excitation/Emission Mechanism, and the Astrophysical Implications. *Astrophys. J. Suppl. Ser.* **1989**, *71*, 733–775.

(3) Peeters, E.; Mackie, C.; Candian, A.; Tielens, A. G. G. M. A Spectroscopic View on Cosmic PAH Emission. *Acc. Chem. Res.* **2021**, *54*, 1921–1933.

(4) Tielens, A. G. G. M. Interstellar Polycyclic Aromatic Hydrocarbon Molecules. *Annu. Rev. Astron. Astrophys.* **2008**, *46*, 289–337.

(5) Li, A. Spitzer's Perspective of Polycyclic Aromatic Hydrocarbons in Galaxies. *Nat. Astron.* **2020**, *4*, 339–351.

(6) Tielens, A. G. G. M. The Molecular Universe. *Rev. Mod. Phys.* **2013**, *85*, 1021–1081.

(7) Ehrenfreund, P.; Rasmussen, S.; Cleaves, J.; Chen, L. Experimentally Tracing the Key Steps in the Origin of Life: The Aromatic World. *Astrobiology* **2006**, *6*, 490–521.

(8) Steele, A. A.; Mccubbin, F. M.; Fries, M.; Kater, L.; Boctor, N. Z.; Fogel, M. L.; Glamoclija, M.; Spencer, M.; Morrow, A. L.; Hammond, M. R.; Zare, R. N.; Siljeström, S.; Bowden, R.; Herd, C. D. K.; Mysen, B. O.; Shirey, S. B.; Treiman, A. H.; Bullock, E. S.; Jull, A. J. T. A Reduced Organic Carbon Component in Martian Basalts. *Science* **2012**, *337*, 212–215.

(9) Moreels, G.; Clairemidi, J.; Hermine, P.; Brechignac, P.; Rousselot, P. Detection of a Polycyclic Aromatic Molecule in Comet P/Halley. *Astron. Astrophys.* **1994**, *282*, 643–656.

(10) Venkataraman, V.; Roy, A.; Ramachandran, R.; Quitián-Lara, H. M.; Hill, H.; RajaSekhar, B. N.; Bhardwaj, A.; Mason, N. J.; Sivaraman, B. Detection of Polycyclic Aromatic Hydrocarbons on a Sample of Comets. *J. Astrophys. Astron.* **2023**, *44*.

(11) Li, A. PAHs in Comets: An Overview. In *ESO Astrophysics Symposia*; 2009; Vol. 2009, pp 161–175.

(12) López-Puertas, M.; Dinelli, B. M.; Adriani, A.; Funke, B.; García-Comas, M.; Moriconi, M. L.; D'Aversa, E.; Boersma, C.; Allamandola, L. J. Large Abundances Of Polycyclic Aromatic Hydrocarbons in Titan's Upper Atmosphere. *Astrophys. J.* **2013**, *770*, 1–8.

(13) Allamandola, L. J.; Sandford, S. A.; Wopenka, B. Interstellar Polycyclic Aromatic Hydrocarbons and Carbon in Interplantary Dust Particles and Meteorites. *Science* **1987**, *237*, 56–59.

(14) Goldsworthy, B. J.; Burchell, M. J.; Cole, M. J.; Armes, S. P.; Khan, M. A.; Lascelles, S. F.; Green, S. F.; McDonnell, J. A. M.; Srama, R.; Bigger, S. W. Time of Flight Mass Spectra of Ions in Plasmas Produced by Hypervelocity Impacts of Organic and Mineralogical Microparticles on a Cosmic Dust Analyser. *Astron. Astrophys.* **2003**, *409*, 1151–1167.

(15) Li, Y. W.; Bugiel, S.; Trieloff, M.; Hillier, J. K.; Postberg, F.; Price, M. C.; Shu, A.; Fiege, K.; Fielding, L. A.; Armes, S. P.; Wu, Y. Y.; Grün, E.; Srama, R. Morphology of Craters Generated by Hypervelocity Impacts of Micron-Sized Polypyrrole-Coated Olivine Particles. *Meteorit. Planet. Sci.* **2014**, *49*, 1375–1387.

(16) Postberg, F.; Kempf, S.; Schmidt, J.; Brilliantov, N.; Beinsen, A.; Abel, B.; Buck, U.; Srama, R. Sodium Salts in E-Ring Ice Grains from an Ocean below the Surface of Enceladus. *Nature* **2009**, *459*, 1098–1101.

(17) Postberg, F.; Khawaja, N.; Abel, B.; Choblet, G.; Glein, C. R.; Gudipati, M. S.; Henderson, B. L.; Hsu, H. W.; Kempf, S.; Klenner, F.; Moragas-Klostermeyer, G.; Magee, B.; Nölle, L.; Perry, M.; Reviol, R.; Schmidt, J.; Srama, R.; Stolz, F.; Tobie, G.; Trieloff, M.; Waite, J. H. Macromolecular Organic Compounds from the Depths of Enceladus. *Nature* **2018**, *558*, 564–568.

(18) Postberg, F.; Sekine, Y.; Klenner, F.; Glein, C. R.; Zou, Z.; Abel, B.; Furuya, K.; Hillier, J. K.;

Khawaja, N.; Kempf, S.; Noelle, L.; Saito, T.; Schmidt, J.; Shibuya, T.; Srama, R.; Tan, S. Detection of Phosphates Originating from Enceladus's Ocean. *Nature* **2023**, *618*, 489–493.

(19) Srama, R.; Ahrens, T. J.; Altobelli, N.; Auer, S.; Bradley, J. G. The Cassini Cosmic Dust Analyzer. *Space Sci. Rev.* **2004**, *114*, 465–518.

(20) Sternovsky, Z.; Amyx, K.; Bano, G.; Landgraf, M.; Horanyi, M.; Knappmiller, S.; Robertson, S.; Grün, E.; Srama, R.; Auer, S. Large Area Mass Analyzer Instrument for the Chemical Analysis of Interstellar Dust Particles. *Rev. Sci. Instrum.* **2007**, *78*, 014501.

(21) Kempf, S.; Tucker, S.; Altobelli, N.; Briois, C.; Cable, M. L.; Grün, E.; Gudipati, M. S.; Henderson, B. L.; Hsu, H. W.; Hand, K.; Horanyi, M.; Postberg, F.; Schmidt, J.; Srama, R.; Sternovsky, Z.; Tobie, G.; Zolotov, M. Y.; Belting, C.; Bortfeldt, S.; Bouwman, J.; Brennan, N.; Bryant, K.; Cassidy, T.; Crotser, D.; Curtin, A.; DeVito, E.; Ebuen, D.; Faber, N.; Fisher, M.; Fontanese, J.; Fowle, M.; Frank, W.; Gurst, S.; Haselschwardt, S.; Hoxie, V.; Hubbell, K.; James, D.; Kien, M.; Knappmiller, S.; Kohnert, R.; Lampe, A.; Lankton, M.; Lev-Tov, S.; McGinn, C.; Miller, M.; Newcomb, G.; Oberg, S.; O'Brien, L.; Pilewskie, K.; Polson, S.; Scarffe-Barrett, V.; Summers, D.; Wade, S.; Ware, A.; Yehle, A.; Wuerthner, C.; Garcia Arteaga, A.; Oaida, B.; Eberl, C.; Fitton, P.; Goode, W.; Levin, Z.; Lowry, G.; Stanley, J.; Tracy, A.; Ulibarri, Z.; Williams, E.; Yoke, C.; Southworth, B. S.; Hillier, J. K.; Khawaja, N.; Klenner, F.; Napoleoni, M.; Simolka, J.; Sioeng, J. SUDA: A SUrface Dust Analyser for Compositional Mapping of the Galilean Moon Europa. *Space Sci. Rev.* **2025**, *221*.

(22) Simolka, J.; Blanco, R.; Ingerl, S.; Krüger, H.; Sommer, M.; Srama, R.; Strack, H.; Wagner, C.; Arai, T.; Bauer, M.; Fröhlich, P.; Gläser, J.; Gräßlin, M.; Henselowsky, C.; Hillier, J.; Hirai, T.; Ito, M.; Kempf, S.; Khawaja, N.; Kimura, H.; Klinkner, S.; Kobayashi, M.; Lengowski, M.; Li, Y.; Mocker, A.; Moragas-Klostermeyer, G.; Postberg, F.; Rieth, F.; Sasaki, S.; Schmidt, J.; Sterken, V.; Sternovsky, Z.; Strub, P.; Szalay, J.; Trieloff, M.; Yabuta, H. The DESTINY + Dust Analyser - a Dust Telescope for Analysing Cosmic Dust Dynamics and Composition. *Philos. Trans. R. Soc. A Math. Phys. Eng. Sci.* **2024**, *382*.

(23) Hörz, F.; Bastien, R.; Borg, J.; Bradley, J. P.; Bridges, J. C.; Brownlee, D. E.; Burchell, M. J.; Chi, M.; Cintala, M. J.; Dai, Z. R.; Djouadi, Z.; Dominguez, G.; Economou, T. E.; Fairey, S. A. J.; Floss, C.; Franchi, I. A.; Graham, G. A.; Green, S. F.; Heck, P.; Hoppe, P.; Huth, J.; Ishii, H.; Kearsley, A. T.; Kissel, J.; Leitner, J.; Leroux, H.; Marhas, K.; Messenger, K.; Schwandt, C. S.; See, T. H.; Snead, C.; Stadermann, F. J.; Stephan, T.; Stroud, R.; Teslich, N.; Trigo-Rodríguez, J. M.; Tuzzolino, A. J.; Troadec, D.; Tsou, P.; Warren, J.; Westphal, A.; Wozniakiewicz, P.; Wright, I.; Zinner, E. Impact Features on Stardust : Implications for Comet 81P/Wild 2 Dust. *Science* **2006**, *314*, 1716–1719.

(24) Kearsley, A. T.; Borg, J.; Graham, G. A.; Burchell, M. J.; Cole, M. J.; Leroux, H.; Bridges, J. C.; Hörz, F.; Wozniakiewicz, P. J.; Bland, P. A.; Bradley, J. P.; Dai, Z. R.; Teslich, N.; See, T.; Hoppe, P.; Heck, P. R.; Huth, J.; Stadermann, F. J.; Floss, C.; Marhas, K.; Stephan, T.; Leitner, J. Dust from Comet Wild 2: Interpreting Particle Size, Shape, Structure, and Composition from Impact Features on the Stardust Aluminum Foils. *Meteorit. Planet. Sci.* **2008**, *43*, 41–73.

(25) Burchell, M. J.; Graham, G.; Kearsley, A. Cosmic Dust Collection in Aerogel. *Annu. Rev. Earth Planet. Sci.* **2006**, *34*, 385–418.

(26) Brownlee, D.; Tsou, P.; Aléon, J.; O'D Alexander, C. M.; Araki, T.; Bajt, S.; Baratta, G. A.; Bastien, R.; Bland, P.; Bleuet, P.; Borg, J.; Bradley, J. P.; Brearley, A.; Brenker, F.; Brennan, S.; Bridges, J. C.; Browning, N. D.; Brucato, J. R.; Bullock, E.; Burchell, M. J.; Busemann, H.; Butterworth, A.; Chaussidon, M.; Cheuvront, A.; Chi, M.; Cintala, M. J.; Clark, B. C.; Clemett, S. J.; Cody, G.; Colangeli, L.; Cooper, G.; Cordier, P.; Daghlian, C.; Dai, Z.; D'Hendecourt, L.; Djouadi, Z.; Dominguez, G.; Duxbury, T.; Dworkin, J. P.; Ebel, D. S.; Economou, T. E.; Fakra, S.; Fairey, S. A. J.; Fallon, S.; Ferrini, G.; Ferroir, T.; Fleckenstein, H.; Floss, C.; Flynn, G.; Franchi, I. A.; Fries, M.; Gainsforth, Z.; Gallien, J. P.; Genge, M.; Gilles, M. K.; Gillet, P.; Gilmour, J.; Glavin, D. P.; Gounelle, M.; Grady, M. M.; Graham, G. A.; Grant, P. G.; Green, S. F.; Grossemy, F.; Grossman, L.; Grossman, J. N.; Guan, Y.; Hagiya, K.; Harvey, R.; Heck, P.; Herzog, G. F.;

Hoppe, P.; Hörz, F.; Huth, J.; Hutcheon, I. D.; Ignatyev, K.; Ishii, H.; Ito, M.; Jacob, D.; Jacobsen, C.; Jacobsen, S.; Jones, S.; Joswiak, D.; Jurewicz, A.; Kearsley, A. T.; Keller, L. P.; Khodja, H.; Kilcoyne, A. L. D.; Kissel, J.; Krot, A.; Langenhorst, F.; Lanzirotti, A.; Le, L.; Leshin, L. A.; Leitner, J.; Lemelle, L.; Leroux, H.; Liu, M. C.; Luening, K.; Lyon, I.; MacPherson, G.; Marcus, M. A.; Marhas, K.; Marty, B.; Matrajt, G.; McKeegan, K.; Meibom, A.; Mennella, V.; Messenger, K.; Messenger, S.; Mikouchi, T.; Mostefaoui, S.; Nakamura, T.; Nakano, T.; Newville, M.; Nittler, L. R.; Ohnishi, I.; Ohsumi, K.; Okudaira, K.; Papanastassiou, D. A.; Palma, R.; Palumbo, M. E.; Pepin, R. O.; Perkins, D.; Perronnet, M.; Pianetta, P.; Rao, W.; Rietmeijer, F. J. M.; Robert, F.; Rost, D.; Rotundi, A.; Ryan, R.; Sandford, S. A.; Schwandt, C. S.; See, T. H.; Schlutter, D.; Sheffield-Parker, J.; Simionovici, A.; Simon, S.; Sitnitsky, I.; Snead, C. J.; Spencer, M. K.; Stadermann, F. J.; Steele, A.; Stephan, T.; Stroud, R.; Susini, J.; Sutton, S. R.; Suzuki, Y.; Taheri, M.; Taylor, S.; Teslich, N.; Tomeoka, K.; Tomioka, N.; Toppani, A.; Trigo-Rodríguez, J. M.; Troadec, D.; Tsuchiyama, A.; Tuzzolino, A. J.; Tyliszczak, T.; Uesugi, K.; Velbel, M.; Vellenga, J.; Vicenzi, E.; Vincze, L.; Warren, J.; Weber, I.; Weisberg, M.; Westphal, A. J.; Wirick, S.; Wooden, D.; Wopenka, B.; Wozniakiewicz, P.; Wright, I.; Yabuta, H.; Yano, H.; Young, E. D.; Zare, R. N.; Zega, T.; Ziegler, K.; Zimmerman, L.; Zinner, E.; Zolensky, M. Comet 81P/Wild 2 under a Microscope. *Science* **2006**, *314*, 1711–1716.

(27) Burchell, M. J.; Fairey, S. A. J.; Wozniakiewicz, P.; Brownlee, D. E.; Hörz, F.; Kearsley, A. T.; See, T. H.; Tsou, P.; Westphal, A.; Green, S. F.; Trigo-Rodríguez, J. M.; Domingúez, G. Characteristics of Cometary Dust Tracks in Stardust Aerogel and Laboratory Calibrations. *Meteorit. Planet. Sci.* **2008**, *43*, 23–40.

(28) Burchell, M. J.; Wozniakiewicz, P. J. Icy Ocean Worlds, Plumes, and Tasting the Water. *Meteorit. Planet. Sci.* **2024**, *59*, 1385–1406.

(29) Lorenz, R. D.; Burk, T. A. Enceladus Plume Density from Cassini Spacecraft Attitude Control Data. *Icarus* **2018**, *300*, 200–202.

(30) Guzman, M.; Lorenz, R.; Hurley, D.; Farrell, W.; Spencer, J.; Hansen, C.; Hurford, T.; Ibea, J.; Carlson, P.; McKay, C. P. Collecting Amino Acids in the Enceladus Plume. *Int. J. Astrobiol.* **2019**, *18*, 47–59.

(31) MacKenzie, S. M.; Neveu, M.; Davila, A. F.; Lunine, J. I.; Cable, M. L.; Phillips-Lander, C. M.; Eigenbrode, J. L.; Waite, J. H.; Craft, K. L.; Hofgartner, J. D.; McKay, C. P.; Glein, C. R.; Burton, D.; Kounaves, S. P.; Mathies, R. A.; Vance, S. D.; Malaska, M. J.; Gold, R.; German, C. R.; Soderlund, K. M.; Willis, P.; Freissinet, C.; McEwen, A. S.; Brucato, J. R.; De Vera, J. P. P.; Hoehler, T. M.; Heldmann, J. Science Objectives for Flagship-Class Mission Concepts for the Search for Evidence of Life at Enceladus. *Astrobiology* **2022**, *22*, 685–712.

(32) Ershova, A.; Schmidt, J.; Postberg, F.; Khawaja, N.; Nölle, L.; Srama, R.; Kempf, S.; Southworth, B. Modeling the Enceladus Dust Plume Based on in Situ Measurements Performed with the Cassini Cosmic Dust Analyzer. *Astron. Astrophys.* **2024**, *689*, 1–22.

(33) Chan, D. H.; Millet, A.; Fisher, C. R.; Price, M. C.; Burchell, M. J.; Armes, S. P. Synthesis and Characterization of Polypyrrole-Coated Anthracene Microparticles: A New Synthetic Mimic for Polyaromatic Hydrocarbon-Based Cosmic Dust. *ACS Appl. Mater. Interfaces* **2021**, *13*, 3175–3185.

(34) Burchell, M. J.; Cole, M. J.; McDonnell, J. A. M.; Zarnecki, J. C. Hypervelocity Impact Studies Using the 2 MV Van de Graaff Accelerator and Two-Stage Light Gas Gun of the University of Kent at Canterbury. *Meas. Sci. Technol.* **1999**, *10*, 41–50.

(35) Mikula, R.; Sternovsky, Z.; Armes, S. P.; Ayari, E.; Bouwman, J.; Chan, D. H. H.; Fontanese, J.; Horanyi, M.; Hillier, J. K.; Kempf, S.; Khawaja, N.; Kupihár, Z.; Postberg, F.; Srama, R. Impact Ionization Mass Spectra of Polypyrrole-Coated Anthracene Microparticles: A Useful Mimic for Cosmic Polycyclic Aromatic Hydrocarbon Dust. *ACS Earth Sp. Sci.* **2024**, *8*, 586–605.

(36) Chan, D. H. H.; Wills, J. L.; Tandy, J. D.; Burchell, M. J.; Wozniakiewicz, P. J.; Alesbrook, L. S.; Armes, S. P. Synthesis of Autofluorescent Phenanthrene Microparticles via Emulsification: A Useful Synthetic Mimic for Polycyclic Aromatic Hydrocarbon-Based Cosmic Dust. *ACS Appl.*

Mater. Interfaces **2023**, *15*, 54039–54049.
(37) Hudgins, D. M.; Bauschlicher, Jr., C. W.; Allamandola, L. J. Variations in the Peak Position of the 6.2 Mm Interstellar Emission Feature: A Tracer of N in the Interstellar Polycyclic Aromatic Hydrocarbon Population. *Astrophys. J.* **2005**, *632*, 316–332.
(38) Canelo, C. M.; Friaça, A. C. S.; Sales, D. A.; Pastoriza, M. G.; Ruschel-Dutra, D. Variations in the 6.2 Mm Emission Profile in Starburst-Dominated Galaxies: A Signature of Polycyclic Aromatic Nitrogen Heterocycles (PANHs)? *Mon. Not. R. Astron. Soc.* **2018**, *475*, 3746–3763.
(39) McGuire, B. A.; Burkhardt, A. M.; Kalenskii, S.; Shingledecker, C. N.; Remijan, A. J.; Herbst, E.; McCarthy, M. C. Detection of the Aromatic Molecule Benzonitrile (c-C6H5CN) in the Interstellar Medium. *Science* **2018**, *359*, 202–205.
(40) Hibbert, R.; Cole, M. J.; Price, M. C.; Burchell, M. J. The Hypervelocity Impact Facility at the University of Kent: Recent Upgrades and Specialized Capabilities. *Procedia Eng.* **2017**, *204*, 208–214.
(41) Brotherton, E. E.; Chan, D. H. H.; Armes, S. P.; Janani, R.; Sammon, C.; Wills, J. L.; Tandy, J. D.; Burchell, M. J.; Wozniakiewicz, P. J.; Alesbrook, L. S.; Tabata, M. Synthesis of Phenanthrene/Pyrene Hybrid Microparticles: Useful Synthetic Mimics for Polycyclic Aromatic Hydrocarbon-Based Cosmic Dust. *J. Am. Chem. Soc.* **2024**, *146*, 20802–20813.
(42) L'Estimé, M.; Schindler, M.; Shahidzadeh, N.; Bonn, D. Droplet Size Distribution in Emulsions. *Langmuir* **2024**, *40*, 275–281.
(43) Burchell, M. J.; Foster, N. J.; Ormond-Prout, J.; Dupin, D.; Armes, S. P. Extent of Thermal Ablation Suffered by Model Organic Microparticles during Aerogel Capture at Hypervelocities. *Meteorit. Planet. Sci.* **2009**, *44*, 1407–1419.
(44) Keyte, I.; Wild, E.; Dent, J.; Jones, K. C. Investigating the Foliar Uptake and Within-Leaf Migration of Phenanthrene by Moss (Hypnum Cupressiforme) Using Two-Photon Excitation Microscopy with Autofluorescence. *Environ. Sci. Technol.* **2009**, *43*, 5755–5761.
(45) Wild, E.; Dent, J.; Barber, J. L.; Thomas, G. O.; Jones, K. C. A Novel Analytical Approach for Visualizing and Tracking Organic Chemicals in Plants. *Environ. Sci. Technol.* **2004**, *38*, 4195–4199.
(46) Qazi, F.; Shahsavari, E.; Prawer, S.; Ball, A. S.; Tomljenovic-Hanic, S. Detection and Identification of Polyaromatic Hydrocarbons (PAHs) Contamination in Soil Using Intrinsic Fluorescence. *Environ. Pollut.* **2021**, *272*, 1–11.
(47) Anyanwu, I. N.; Semple, K. T. Fate and Behaviour of Nitrogen-Containing Polycyclic Aromatic Hydrocarbons in Soil. *Environ. Technol. Innov.* **2015**, *3*, 108–120.
(48) In the context of the present study, an indentation is slight flexure in the target surface, whereas a crater is associated with the spatial redistribution of material.
(49) New, J. S.; Mathies, R. A.; Price, M. C.; Cole, M. J.; Golozar, M.; Spathis, V.; Burchell, M. J.; Butterworth, A. L. Characterizing Organic Particle Impacts on Inert Metal Surfaces: Foundations for Capturing Organic Molecules during Hypervelocity Transits of Enceladus Plumes. *Meteorit. Planet. Sci.* **2020**, *55*, 465–479.
(50) Burke, S. E.; Continetti, R. E. Submicrometer Particle Impact Dynamics and Chemistry. *Annu. Rev. Phys. Chem.* **2024**, *75*, 67–88.
(51) Fisher, C. R.; Price, M. C.; Burchell, M. J. Salt Grains in Hypervelocity Impacts in the Laboratory: Methods to Sample Plumes from the Ice Worlds Enceladus and Europa. *Meteorit. Planet. Sci.* **2021**, *56*, 1652–1668.
(52) Melosh, H. J. The Contact and Compression Stage of Impact Cratering. In *Impact Cratering: Processes and Products*; Osinski, G. R., Pierazzo, E., Eds.; Wiley-Blackwell: Chichester, 2012; pp 32–42.
(53) Marsh, S. P. *LASL Shock Hugoniot Data*; University of California Press: Los Angeles, 1980.
(54) Anderson, W. W. *Physics of Interplanetary Dust Collection with Aerogel. NASA/CR-1998-207766; Georgia Southwestern State University: GA*; 1998.
(55) Artemieva, N.; Ivanov, B. Launch of Martian Meteorites in Oblique Impacts. *Icarus* **2004**, *171*,

87–101.
(56) Fritz, J.; Artemieva, N.; Greshake, A. Ejection of Martian Meteorites. *Meteorit. Planet. Sci.* **2005**, *40*, 1393–1411.
(57) Steele, W. V.; Chirico, R. D.; Hossenlopp, I. A.; Nguyen, A.; Smith, N. K.; Gammon, B. E. The Thermodynamic Properties of the Five Benzoquinolines. *J. Chem. Thermodyn.* **1989**, *21*, 81–107.
(58) Finke, H. L.; Messerly, J. F.; Lee, S. H.; Osborn, A. G.; Douslin, D. R. Comprehensive Thermodynamic Studies of Seven Aromatic Hydrocarbons. *J. Chem. Thermodyn.* **1977**, *9*, 937–956.
(59) Kitazawa, Y.; Fujiwara, A.; Kadono, T.; Imagawa, K.; Okada, Y.; Uematsu, K. Hypervelocity Impact Experiments on Aerogel Dust Collector. *J. Geophys. Res. Planets* **1999**, *104*, 22035–22052.
(60) Burchell, M. J.; Fairey, S. A. J.; Foster, N. J.; Cole, M. J. Hypervelocity Capture of Particles in Aerogel: Dependence on Aerogel Properties. *Planet. Space Sci.* **2009**, *57*, 58–70.
(61) In reality, PAH- and PANH-based cosmic dust will almost certainly comprise a complex mixture of such aromatic molecules, rather than the simple benzo[*h*]quinoline or benzo[*h*]quinoline/phenanthrene hybrid microparticles reported herein.